IRIS AperTO

UNIVERSITÀ DEGLI STUDI DI TORINO

AperTO - Archivio Istituzionale Open Access dell'Università di Torino

Tuning Carbon Dioxide Adsorption Affinity of Zinc(II) MOFs by Mixing Bis(pyrazolate) Ligands with N-Containing Tags

This is a pre print version of the following article:

Original Citation:

Availability:

This version is available http://hdl.handle.net/2318/1730481 since 2020-02-24T16:06:45Z

Published version:

DOI:10.1021/acsami.9b08015

Terms of use:

Open Access

Anyone can freely access the full text of works made available as "Open Access". Works made available under a Creative Commons license can be used according to the terms and conditions of said license. Use of all other works requires consent of the right holder (author or publisher) if not exempted from copyright protection by the applicable law.

(Article begins on next page)

15 December 2021

Tuning carbon dioxide adsorption affinity of zinc(II) MOFs by mixing bis(pyrazolate) ligands with N-containing tags

Rebecca Vismara,[a] *Giulia Tuci,*[b] *Alessia Tombesi,*[c] *Konstantin V. Domasevitch,*[d] *Corrado Di Nicola,*[e]

Giuliano Giambastiani,[b,f,g] *Michele R. Chierotti,*[h] *Simone Bordignon,*[h] *Roberto Gobetto,*[h]

Claudio Pettinari,[c] *Andrea Rossin*[b,f,*] *and Simona Galli*[a,f,*]

[a] Dipartimento di Scienza e Alta Tecnologia, Università dell'Insubria,
Via Valleggio 11, 22100 Como, Italy.

[b] Istituto di Chimica dei Composti Organometallici (ICCOM-CNR),
Via Madonna del Piano 10, 50019 Sesto Fiorentino (Firenze), Italy.

[c] Scuola del Farmaco e dei Prodotti della Salute, Università di Camerino,
Via S. Agostino 1, 62032 Camerino, Italy.

[d] Taras Shevchenko National University of KyivVolodymyrska Str. 64/13, 01601 Kyiv, Ukraine.

[e] Scuola di Scienze e Tecnologie, Università di Camerino,
Via S. Agostino 1, 62032 Camerino, Italy.

[f] Consorzio Interuniversitario Nazionale per la Scienza e Tecnologia dei Materiali,
Via Giusti 9, 50121 Firenze, Italy.

[g] Institute of Chemistry and Processes for Energy, Environment and Health (ICPEES), UMR 7515 CNRS-University of Strasbourg (UdS), 25, rue Becquerel, 67087 Strasbourg Cedex 02, France.

[h] Department of Chemistry and NIS Centre, University of Torino,
Via Giuria 7, 10125, Torino, Italy.

Authors to whom correspondence should be addressed: simona.galli@uninsubria.it; a.rossin@iccom.cnr.it.

Abstract. The four zinc(II) mixed-ligand MOFs (MIXMOFs) $Zn(BPZ)_x(BPZNO_2)_{1-x}$, $Zn(BPZ)_x(BPZNH_2)_{1-x}$, $Zn(BPZNO_2)_x(BPZNH_2)_{1-x}$ and $Zn(BPZ)_x(BPZNO_2)_y(BPZNH_2)_{1-x-y}$ (H_2BPZ = 4,4'-bipyrazole; H_2BPZNO_2 = 3-nitro-4,4'-bipyrazole; H_2BPZNH_2 = 3-amino-4,4'-bipyrazole) were prepared through solvothermal routes and fully investigated in the solid state. Isoreticular to the end-members Zn(BPZ) and Zn(BPZX) (X = NO_2, NH_2), they are the first examples ever reported of (pyr)azolate MIXMOFs. Their crystal structure is characterized by a 3-D open framework with 1-D square or rhombic channels decorated by the functional groups. Accurate information about ligand stoichiometric ratio was determined (for the first time on MIXMOFs) through integration of selected ligands skeleton resonances from ^{13}C CPMAS solid-state NMR spectra collected on the as-synthesized materials. Like other poly(pyrazolate) MOFs, the four MIXMOFs are thermally stable, with decomposition temperatures between 708 and 726 K. As disclosed by N_2 adsorption at 77 K, they are micro-mesoporous materials with BET specific surface areas in the range 400-600 m^2/g. A comparative study (involving also the single-ligand analogues) of CO_2 adsorption capacity, CO_2 isosteric heat of adsorption (Q_{st}) and CO_2/N_2 selectivity in equimolar mixtures at p = 1 bar and T = 298 K casted light on interesting trends, depending on ligand tag nature or ligand stoichiometric ratio. In particular, the amino-decorated compounds show higher Q_{st} values and CO_2/N_2 selectivity *vs.* the nitro functionalized analogues; in addition, tag "dilution" [upon passing from Zn(BPZX) to $Zn(BPZ)_x(BPZX)_{1-x}$] increases CO_2 adsorption selectivity over N_2. The simultaneous presence of amino and nitro groups is not beneficial for CO_2 uptake. Among the compounds studied, the best compromise among uptake capacity, Q_{st} and CO_2/N_2 selectivity is represented by $Zn(BPZ)_x(BPZNH_2)_{1-x}$.

Keywords

Mixed-ligand Metal-Organic Frameworks (MIXMOFs) – zinc – carbon dioxide – porous materials – nitrogen ligands – carbon capture and sequestration (CCS) – ^{13}C CPMAS NMR spectroscopy – ^{15}N CPMAS NMR spectroscopy

Introduction

In the past twenty years, metal-organic frameworks (MOFs)[1] have emerged as a promising alternative to all-inorganic compounds in applications requiring porous materials. Their topology, pore size and pore-wall decoration depend on the stereochemical requirements of the metal ion and the hapticity, size and functionalization of the ligand. When coupled with enhanced thermal and chemical stability, permanent porosity makes MOFs appealing for a number of practical applications.[2] Among these, the so-called Carbon Capture and Sequestration (CCS) technology is rapidly gaining increasing attention in the Worldwide community.[3] Reduction of the CO_2 content in the atmosphere is of fundamental importance to mitigate the consequences of the greenhouse effect and the associated global warming. From this viewpoint, the quest for novel and efficient CO_2 sponges is imperative and several solutions have been proposed in the past.[4] MOFs are a valid category of CO_2 sorbents at mild temperature and pressure conditions. An interesting sub-class of MOFs is represented by Multivariate MOFs or MIXMOFs.[5] Those MIXMOFs incorporating linkers with the same skeleton but bearing different functional groups (tags) grant pore walls heterogeneity,[6] preserving at the same time the structural topology of the parent homologue. Since their discovery, MIXMOFs represent an important milestone in the path toward increased MOF complexity, as their chemico-physical properties are not the simple, linear combination of those of the single-linker analogues. Indeed, MIXMOFs greatly expand the possibility of discovering high-performing adsorbents for environmental applications such as CO_2 capture. Their intrinsic heterogeneity enhances selectivity for carbon dioxide adsorption relative to mixtures of pure materials, as proven by seminal literature works appeared in 2010 and 2013.[7] Recent computational studies carried out on a wide range of MIXMOFs built *in silico* and tested as CO_2 adsorbents[8] have confirmed that many aromatic heterocycles show larger CO_2 affinity than the benzene ring. Thus, the use of heterocyclic linkers should in principle improve MOFs CO_2 sorption capacity. Among the various heterocycles conceivable, poly(azolate) spacers have gained the stage[9] as an alternative to poly(carboxylates) in the synthesis of functional MOFs. In this context, we[10] and others[11] have contributed to the development of the class of poly(pyrazolate)

MOFs. We have recently reported on the synthesis and applications in CO_2 adsorption of MOFs bearing tagged bis(pyrazolate) spacers, namely: $M(BPZNO_2)$[12] (M = Co, Cu, Zn; H_2BPZNO_2 = 3-nitro-4,4'-bipyrazole, Scheme 1) and $M(BPZNH_2)$[13] (M = Ni, Cu, Zn; H_2BPZNH_2 = 3-amino-4,4'-bipyrazole, Scheme 1). The two zinc(II) compounds adsorb 19.4 and 13.5 wt % CO_2 at 298 K and 1 bar, respectively. In view of these encouraging results, we extended the same synthetic protocol to the preparation of the MIXMOFs $Zn(BPZ)_x(BPZNO_2)_{1-x}\cdot n$DMF (**Zn-H/$NO_2$·S**; H_2BPZ = 4,4'-bipyrazole, Scheme 1; DMF = *N*,*N*-dimethylformamide), $Zn(BPZ)_x(BPZNH_2)_{1-x}\cdot n$DMF (**Zn-H/$NH_2$·S**), $Zn(BPZNO_2)_x(BPZNH_2)_{1-x}\cdot n$DMF (**Zn-$NO_2$/$NH_2$·S**) and $Zn(BPZ)_x(BPZNO_2)_y(BPZNH_2)_{1-x-y}\cdot n$DMF (**Zn-H/$NO_2$/$NH_2$·S**), with the aim of finely tuning the CO_2 adsorption capacity and selectivity by varying the quantity and type of ligand functionalization. An accurate quantification of the ligand stoichiometric ratio was carried out on the as-synthesized samples by exploiting solid-state ^{13}C CPMAS NMR spectroscopy, instead of applying the "classical" digestion protocol followed by ^1H NMR analysis in solution. The carbon dioxide adsorption capacity, thermodynamic affinity (in terms of isosteric heat of adsorption, Q_{st}) and CO_2/N_2 selectivity of the title MIXMOFs were compared with those of their single-ligand analogues Zn(BPZ)[14] and Zn(BPZX) (X = NO_2, NH_2). To the best of our knowledge, this is the first example of synthesis and characterization of (pyr)azolate MIXMOFs and the first systematic experimental correlation between CO_2 adsorption capacity and (pyr)azolate MIXMOFs composition.

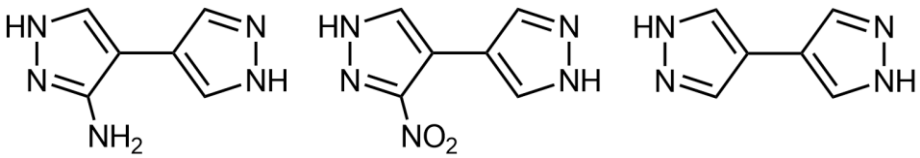

Scheme 1. Molecular structure of the three ligands used in this study: 3-amino-4,4'-bipyrazole (H_2BPZNH_2, left), 3-nitro-4,4'-bipyrazole (H_2BPZNO_2, centre) and 4,4'-bipyrazole (H_2BPZ, right).

Experimental Section

Materials and Methods. All the chemicals and reagents employed were purchased from commercial suppliers and used as received without further purification. 4,4'-Bipyrazole,[15] 3-nitro-4,4'-bipyrazole,[12] 3-amino-4,4'-bipyrazole,[13] Zn(BPZ),[14] Zn(BPZNO$_2$)[12] and Zn(BPZNH$_2$)[13] were synthesized according to previously published procedures. IR spectra were recorded as neat from 4000 to 600 cm^{-1} with a PerkinElmer Spectrum One System instrument. Elemental analyses (C, H, N) were performed with a Fisons Instruments 1108 CHNS-O elemental analyser. Thermogravimetric analysis (TGA) and differential scanning calorimetry (DSC) were carried out simultaneously using a NETZSCH STA 409 PC instrument. 10 mg of as-synthesised samples were placed in alumina crucibles; the temperature programme ranged from 303 to 1173 K with a heating rate of 10 K min^{-1} and under a N_2 flow (40 mL min^{-1}). Raw data from TGA and DSC were corrected based on a background curve. Powder X-ray diffraction (PXRD) data to carry out qualitative analyses were acquired with a Bruker AXS D8 Advance diffractometer (consult the section detailing on the characterization of the crystal and molecular structure for the instrument specifics), working at room temperature in the 2θ range 4.0–35.0°, with steps of 0.02°, and time per step of 1 s. The nature and purity of the batches used for the thermal, NMR and functional characterization were evaluated upon combining elemental analysis, IR spectroscopy and PXRD. FIB-SEM (Focused Ion Beam-Scanning Electron Microscopy) analysis was carried out with a Gaia 3 microscope (Tescan s.r.o, Brno, Czech Republic) on samples previously coated with gold. The electron beam used for SEM imaging had a 20 kV voltage. The instrument operated in high-vacuum mode and with a secondary electron (SE) detector.

Synthesis of Zn(BPZ)$_x$(BPZNO$_2$)$_{1-x}$·*n*DMF (Zn-H/NO$_2$·S). H_2BPZNO$_2$ (0.036 g, 0.20 mmol) and H_2BPZ (0.027 g, 0.20 mmol) were dissolved in DMF (10 mL). Then, Zn(OAc)$_2$·2H$_2$O (0.088 g, 0.40 mmol) (OAc = acetate) was added and the mixture was left under stirring in a high-pressure glass tube at 120 °C for 24 h, until a yellow precipitate appeared. The precipitate was filtered off,

washed with hot acetone (2 × 10 mL) and dichloromethane (2 × 10 mL), and dried under vacuum. Yield 74%. **Zn-H/NO_2·S** is insoluble in dimethylsulfoxide (DMSO), alcohols, acetone, acetonitrile (CH_3CN), chlorinated solvents and water. Elemental analysis calculated for $Zn(BPZ)_{0.64}(BPZNO_2)_{0.36}$·0.75(DMF) (FW = 268.5 g/mol): C, 36.90; H, 3.34; N, 26.66%. Found: C, 36.79; H, 3.51; N, 26.29%. IR (cm^{-1}; Figure 1): 3130, 3098 (vw) [ν(C-H)], 2927 (vw) [$\nu(C-H)_{DMF}$], 1667 (s) [$\nu(C=O)_{DMF}$], 1504 (s) [ν(C=C + C=N)], 1386 (s), 1346 (s) [$\nu_{sym}(NO_2)$], 1267 (s), 1196 (w), 1170 (w), 1104 (s) [ν(C-N)], 1059 (s), 943 (s), 918 (s), 856 (s), 829 (s), 637 (s).

Synthesis of $Zn(BPZ)_x(BPZNH_2)_{1-x}$·*n*DMF (Zn-H/NH_2·S). H_2BPZNH_2 (0.074 g, 0.50 mmol) and H_2BPZ (0.067 g, 0.50 mmol) were dissolved in DMF (10 mL). Then, $Zn(OAc)_2·2H_2O$ (0.219 g, 1.00 mmol) was added and the mixture was left under stirring in a high-pressure glass tube at 120 °C for 3 h, until a white precipitate appeared. The precipitate was filtered off, washed with hot acetone (2 × 10 mL) and dichloromethane (2 × 10 mL), and dried under vacuum. Yield 81%. **Zn-H/NH_2·S** is insoluble in DMSO, alcohols, acetone, CH_3CN, chlorinated solvents and water. Elemental analysis calculated for $Zn(BPZ)_{0.56}(BPZNH_2)_{0.44}$·(DMF) (FW = 277.2 g/mol): C, 38.99; H, 4.16; N, 27.49%. Found: C, 38.87; H, 4.17; N, 27.70%. IR (cm^{-1}; Figure S1): 3390 (m), 3317 (m) [ν(N-H)], 3095 (vw) [ν(C-H)], 2930 (vw) [$\nu(C-H)_{DMF}$], 1658 (vs) [$\nu(C=O)_{DMF}$], 1507 (s) [ν(C=C + C=N)], 1435 (m), 1385 (s), 1265 (s), 1168 (m), 1133 (m), 1091 (s) [ν(C-N)], 1058 (s), 1016 (m), 949 (s), 917 (s), 842 (m).

Synthesis of $Zn(BPZNO_2)_x(BPZNH_2)_{1-x}$·*n*DMF (Zn-$NO_2$/$NH_2$·S). H_2BPZNH_2 (0.075 g, 0.50 mmol) and H_2BPZNO_2 (0.089 g, 0.50 mmol) were dissolved in DMF (20 mL). Then, $Zn(OAc)_2·2H_2O$ (0.219 g, 1.00 mmol) was added and the mixture was left under stirring in a high-pressure glass tube at 120 °C for 3 h, until a yellow precipitate appeared. The precipitate was filtered off, washed with DMF (2 × 10 mL) and dried under vacuum. Yield 78%. **Zn-NO_2/NH_2·S**

is insoluble in DMSO, alcohols, acetone, CH_3CN, chlorinated solvents and water. Elemental analysis calculated for $Zn(BPZNO_2)_{0.34}(BPZNH_2)_{0.66}\cdot 0.85(DMF)$ (FW = 284.9 g/mol): C, 36.04; H, 3.64; N, 28.77%. Found: C, 36.10; H, 3.74; N, 28.82%. IR (cm^{-1}; Figure S2): 3390 (w), 3314 (w) [ν(N-H)], 3098 (w) [ν(C-H)], 2927 (w) [$\nu(C\text{-}H)_{DMF}$], 2871 (w), 1656 (vs) [$\nu(C{=}O)_{DMF}$], 1505 (s) [ν(C=C + C=N)], 1434 (m), 1384 (s), 1346 (s) [$\nu_{sym}(NO_2)$], 1273 (s), 1169 (m), 1132 (m), 1091 (s) [ν(C-N)], 1058 (s), 1012 (m), 943 (s), 917 (m), 842 (m), 827 (m), 657 (m).

Synthesis of $Zn(BPZ)_x(BPZNO_2)_y(BPZNH_2)_{1-x-y}\cdot n$DMF (Zn-H/$NO_2$/$NH_2$·S). H_2BPZ (0.045 g, 0.33 mmol), H_2BPZNH_2 (0.050 g, 0.33 mmol) and H_2BPZNO_2 (0.060 g, 0.33 mmol) were dissolved in DMF (20 mL). Then, $Zn(OAc)_2\cdot 2H_2O$ (0.219 g, 1.00 mmol) was added and the mixture was left under stirring in a high-pressure glass tube at 120 °C for 3 h, until a yellow precipitate appeared. The precipitate was filtered off, washed with DMF (2 × 10 mL) and dried under vacuum. Yield 75%. **Zn-H/NO_2/NH_2·S** is insoluble in DMSO, alcohols, acetone, CH_3CN, chlorinated solvents and water. Elemental analysis calculated for $Zn(BPZ)_{0.49}(BPZNO_2)_{0.28}(BPZNH_2)_{0.23}\cdot 0.75(DMF)$ (FW = 268.4 g/mol): C, 36.92; H, 3.46; N, 27.46%. Found: C, 36.98; H, 3.85; N, 27.23%. IR (cm^{-1}; Figure S2): 3394 (w), 3316 (w) [ν(N-H)], 3098 (w) [ν(C-H)], 2928 (w) [$\nu(C\text{-}H)_{DMF}$], 2868 (w), 1656 (vs) [$\nu(C{=}O)_{DMF}$], 1505 (s) [ν(C=C + C=N)], 1434 (m), 1384 (s), 1346 (m) [$\nu_{sym}(NO_2)$], 1265 (m), 1168 (m), 1133 (m), 1090 (m) [ν(C-N)], 1056 (s), 1013 (m), 943 (m), 917 (m), 845 (m), 828 (m), 657 (m).

Solid-state NMR Characterization and Ligand Stoichiometry Assessment. The ^{13}C and ^{15}N CPMAS NMR spectra of all compounds were acquired with a Jeol ECZR 600 instrument, operating at 600.17, 150.91 and 60.81 MHz for ^{1}H, ^{13}C and ^{15}N nuclei, respectively. The powder samples were packed into a cylindrical zirconia rotor with a 3.2 mm external diameter and a 60 μL volume. 50 mg of as-synthesized sample were used without further manipulations to fill the

rotor. The ^{13}C and ^{15}N CPMAS NMR spectra were acquired at room temperature, at a spinning speed of 20 (^{13}C) and 12 (^{15}N) kHz, using a ramp cross-polarization pulse sequence with a 90° ^{1}H pulse of 2.1 μs, and a contact time of 3.5 (^{13}C) and 4.0 (^{15}N) ms. An optimized recycle delay between 1.0 and 2.5 s was used, for a number of scans in the range 160-2600 (^{13}C) and 29000-164000 (^{15}N), depending on the sample. For each spectrum, a two-pulse phase modulation (TPPM) decoupling scheme was used, with a radiofrequency field of 108.5 kHz. The ^{13}C and ^{15}N chemical shift scales were calibrated against proper signals of the external standard glycine (^{13}C methylenic signal at δ_C = 43.7 ppm and ^{15}N signal at δ_N = 33.4 ppm with respect to NH_3). The stoichiometric coefficients x and y in the molecular formulae $Zn(BPZX)_x(BPZY)_{1-x}$ and $Zn(BPZ)_x(BPZNO_2)_y(BPZNH_2)_{1-x-y}$ were calculated from the ^{13}C NMR signal integrals of C4 and C4' (Scheme 2): the integral values (extracted directly from the signals or after deconvolution) were used to build systems of equations with x and y as variables. The stoichiometric coefficients were then transformed into percentage amounts (%) through simple proportions. The ^{1}H MAS spectra of all compounds were acquired with a Bruker Avance II 400 Ultra Shield instrument, operating at 400.23 MHz for the ^{1}H nuclei. Powder samples were packed into cylindrical zirconia rotors with a 2.5 mm o.d. and a 14 μL volume. 50 mg of sample were used without further preparations to fill the rotor. The spectra were acquired at room temperature at a spinning speed of 32 kHz using a depth sequence, with a 90° ^{1}H pulse of 2.5 μs, optimized recycle delays of ca. 0.4-1.6 s and 16 scans. The ^{1}H chemical shift scale was calibrated through the ^{1}H signal of the external standard adamantane (at 1.87 ppm).

Powder X-ray Diffraction Structural Characterization. Microcrystalline powders of the four MIXMOFs were deposited in the cavity of a silicon free-background plate 0.2 mm deep. Data acquisitions for **Zn-H/NO_2·S** and **Zn-H/NO_2/NH_2·S** were carried out on a vertical-scan Bruker AXS D8 Advance θ:θ diffractometer, equipped with an X-ray tube (CuKα, λ = 1.5418 Å), a Bruker Lynxeye linear position-sensitive detector, a nickel filter in the diffracted beam and the optical components listed in the following: fixed divergence slit (0.5°), primary beam Soller slits

(2.5°), antiscatter slit (8 mm). The generator was run at 40 kV and 40 mA. On the other hand, to acquire the data for **Zn-H/NH_2·S** and **Zn-NO_2/NH_2·S** a vertical-scan Rigaku Miniflex θ:2θ diffractometer was employed, equipped with an X-ray tube (CuKα, λ = 1.5418 Å), a Dtex linear position-sensitive detector, a nickel filter in the diffracted beam and the following optics: fixed divergence slit (1.25°), primary beam Soller slits (2.5°), antiscatter slit (4 mm). The generator was run at 30 kV and 10 mA. After preliminary acquisitions for qualitative analysis, generally performed in the 2θ range 4–35°, diffraction data sets for a complete structural characterization were collected in the 2θ range 5-105°, with steps of 0.02°, with an overall scan time of approximately 12 hours. Comparison of the PXRD pattern of the four MIXMOFs with that of Zn(BPZ)[14] suggested that all the compounds share the same structural motif, though with either tetragonal (*P*4_2/*mmc*) or orthorhombic (*Cccm*) metric. A peak search, followed by profile fitting, enabled us to estimate the low-to-medium-angle peak maximum positions which, through the Singular Value Decomposition algorithm[16] implemented in TOPAS-Academic V6,[17] provided approximate unit cell parameters for all the compounds. Space groups were assigned based on the observed systematic absences. Structure refinement of the framework was carried out with the Rietveld method as implemented in TOPAS-Academic V6,[17] starting from the crystal structure of the parent Zn(BPZ) MOF,[14] and adopting, to define ligand stoichiometry, the ideal values derived from the reaction molar ratios. A rigid body was used to model the ligand independent portion, at first assigning mean values to bond distances and angles.[18] Its orientation (if allowed by symmetry) and the orientation of the NO_2 group with respect to the ligand plane were let vary, while the NH_2 group was left co-planar to the ligand. The center of mass of the ligand lays on a special position. This occurrence means that the NO_2/NH_2 moiety can occupy 1 out of 4 equivalent positions (the 4 carbon atoms of the two pyrazolate rings). The same also holds for the vicariate hydrogen atoms. To locate the solvent, structure solution was then performed with TOPAS-Academic V6 by a combined Monte Carlo/Simulated Annealing approach. A rigid body was used to model DMF,[18] letting its site occupation factor, its orientation and its centre of mass position

vary. During the final Rietveld refinement stages, the site occupation factor of the ligands was refined without restraints, reaching values comparable to those retrieved by ^{13}C CPMAS NMR (Table 1). In addition, ligand bond distances (except the C/N-H distances) were refined in a restrained range of values. In all cases, the background was modelled by a polynomial function of the Chebyshev type. A common, refined isotropic thermal factor (B_{iso}) was attributed to all atoms, except to the metal centres, to which the isotropic thermal factor $B_{iso}(M) = B_{iso}–2.0$ (Å^2) was assigned. The peak profile was described by the Fundamental Parameters Approach.[19] For **Zn-H/NO$_2$·S**, **Zn-NO$_2$/NH$_2$·S** and **Zn-H/NO$_2$/NH$_2$·S**, anisotropic peak broadening was successfully described using the Stephens approach.[20] On the other hand, for **Zn-H/NH$_2$·S**, the broader [*hkl*] and sharper [*h0l*] Bragg reflections were described convoluting two different tan(θ)-dependent spherical harmonics. For all the compounds a Gaussian contribution further lowered the R_{wp} figure of merit. The final stages of the Rietveld refinements are graphically provided in Figure S3 of the Electronic Supplementary Information. The pertinent CIF files are supplied as Electronic Supplementary Information.

Crystal data for **Zn-H/NO$_2$·S**: $Zn(BPZ)_{0.62}(BPZNO_2)_{0.38}·1.7(DMF)$, $C_{11.1}H_{15.5}N_{6.1}O_{2.5}Zn$, FW = 338.90 g mol^{-1}, tetragonal, $P4_2/mmc$, a = 8.9385(6) Å, c = 7.3662(6) Å, V = 588.53(9) Å^3, Z = 16, Z' = 2, ρ = 1.854 g cm^{-3}, $F(000)$ = 348.7, R_{Bragg} = 0.012, R_p = 0.037 and R_{wp} = 0.049, for 4851 data and 34 parameters in the 8.0-105.0° (2θ) range. CCDC No. 1912137.

Crystal data for **Zn-H/NH$_2$·S**: $Zn(BPZ)_{0.56}(BPZNH_2)_{0.44}·1.2(DMF)$, $C_{9.6}H_{12.8}N_{5.6}O_{1.2}Zn$, FW = 291.85 g mol^{-1}, tetragonal, $P4_2/mmc$, a = 8.9805(4) Å, c = 7.3015(5) Å, V = 588.87(5) Å^3, Z = 16, Z' = 2, ρ = 1.687 g cm^{-3}, $F(000)$ = 299.0, R_{Bragg} = 0.014, R_p = 0.033 and R_{wp} = 0.043, for 4901 data and 35 parameters in the 7.0-105.0° (2θ) range. CCDC No. 1912135.

Crystal data for **Zn-NO$_2$/NH$_2$·S**: $Zn(BPZNO_2)_{0.38}(BPZNH_2)_{0.62}·0.8(DMF)$, $C_{8.4}H_{9.8}N_{5.8}O_{1.6}Zn$, FW = 282.41 g mol^{-1}, orthorhombic, *Cccm*, a = 12.528(4) Å, b = 12.776(4) Å, c = 7.360(6) Å, V = 1178(5) Å^3, Z = 16, Z' = 4, ρ = 1.597 g cm^{-3}, $F(000)$ = 573.3, R_{Bragg} = 0.013, R_p = 0.026 and R_{wp} = 0.034, for 4851 data and 37 parameters in the 8.0-105.0° (2θ) range. CCDC No. 1912138.

Crystal data for **Zn-H/NO_2/NH_2·S**: $Zn(BPZ)_{0.46}(BPZNO_2)_{0.33}(BPZNH_2)_{0.21}\cdot 1.2(DMF)$, $C_{9.6}H_{12.3}N_{5.7}O_{1.9}Zn$, FW = 303.25 g mol^{-1}, orthorhombic, *Cccm*, *a* = 12.791(3) Å, *b* = 12.516(3) Å, *c* = 7.3533(7) Å, *V* = 1177.2(4) $Å^3$, *Z* = 16, *Z*' = 4, ρ = 1.710 g cm^{-3}, *F*(000) = 619.8, R_{Bragg} = 0.008, R_p = 0.023 and R_{wp} = 0.031, for 4851 data and 37 parameters in the 8.0-105.0° (2θ) range. CCDC No. 1912136.

Variable-Temperature Powder X-ray Diffraction. To complement the simultaneous thermal analysis, the thermal behaviour of the four MIXMOFs was investigated in situ by variable-temperature powder X-ray diffraction. Using a custom-made sample heater (Officina Elettrotecnica di Tenno, Ponte Arche, Italy), 20-mg samples of the as-synthesized compounds were heated in air from 303 K up to 763 K (the highest temperature reached by the instrument), with 20 K steps; a PXRD pattern was measured for each step within a sensible 2θ range at low-to-medium angles. The unit cell parameters variation as a function of the temperature was disclosed by means of Le Bail parametric refinements of the data measured before observing crystallinity loss.

Stability *vs.* Water Vapor. To check the stability of MIXMOF samples towards water vapor, 15 mg of sample were deposited in the hollow of an aluminum sample-holder. Preliminary PXRD data were acquired with the diffractometer described above in the 2θ range 5-35°, with steps of 0.02° and time per step of 1 s. Then, the sample holder was introduced into an air-tight water-vapor saturated cell. At different time points, each sample was checked by PXRD, adopting the same conditions employed for the preliminary acquisition.

N_2 and CO_2 Adsorption. All the samples were activated at 393 K under high vacuum (10^{-6} Torr) for 24 h before any measurement. The Brunauer−Emmett−Teller (BET) specific surface

area and porosity were estimated by volumetric adsorption with an ASAP 2020 Micromeritics instrument, using N_2 as adsorbate at 77 K. A typical measurement used 40 mg of sample. For the BET specific surface area calculation, the 0.01-0.1 p/p_0 pressure range was used to fit the data. Within this range, all the Rouquerol consistency criteria[21] are satisfied. The micropore area was estimated by means of the *t*-plot method, adopting the Harkins and Jura thickness equation, while the micropore volume was estimated through the application of the Dubinin-Astakhov model to the N_2 isotherm in the $0 \leq p/p_0 \leq 0.02$ range.[22] CO_2 adsorption isotherms were measured at 273 and 298 K up to the maximum pressure of 1.2 bar. The isosteric heat of adsorption (Q_{st}) was calculated working on the CO_2 isotherms measured at 273 and 298 K, by applying a variant of the Clausius-Clapeyron equation (Equation 1):[23]

$$\ln\left(\frac{p_1}{p_2}\right) = Q_{st} \times \frac{T_2 - T_1}{R \times T_1 \times T_2} \qquad \text{(Equation 1)}$$

where p_n (n = 1 or 2) denotes the pressure value for the n^{th} isotherm; T_n (n = 1 or 2) denotes the temperature value for the n^{th} isotherm; R is the gas constant expressed in the appropriate units (8.314 J K^{-1} mol^{-1}). To evaluate the CO_2/N_2 selectivity at 298 K, the N_2 adsorption isotherms were acquired at 298 K and up to 1.2 bar. The CO_2/N_2 selectivity was calculated through the Henry method as the ratio of the initial slopes of the two adsorption isotherms. The IAST selectivity for an equimolar mixture of CO_2 and N_2 at a total pressure of 1 bar was determined as the ratio of the (adsorbed) molar fractions of the two gases[24] by applying the free software pyIAST (https://github.com/CorySimon/pyIAST) to the measured isotherms. A BET (CO_2) and a Henry (N_2) model were employed for the isotherm fitting. For a detailed explanation of these models, see the pyIAST webpage and documentation.

Results and Discussion

(a) Synthesis and Infrared Spectroscopy Characterization. Microcrystalline samples of the MIXMOFs **Zn-H/NO_2·S**, **Zn-H/NH_2·S**, **Zn-NO_2/NH_2·S** and **Zn-H/NO_2/NH_2·S** were obtained in a straightforward manner under the same experimental conditions used to prepare the single-ligand

homologues Zn(BPZNO$_2$)·S[12] and Zn(BPZNH$_2$)·S,[13] namely: upon reacting Zn(OAc)$_2$·2H$_2$O (OAc = acetate) and the proper ligands in DMF under solvothermal conditions, without an auxiliary base to deprotonate the spacers. IR spectroscopy[25] (Figures 1, S1 and S2) is diagnostic of *i*) the incorporation of the functionalized ligands (NO_2 symmetric stretching band centred at 1346, 1345 and 1347 cm^{-1} in **Zn-H/NO$_2$·S**, **Zn-NO$_2$/NH$_2$·S** and **Zn-H/NO$_2$/NH$_2$·S**, respectively; NH_2 stretching bands in the range 3317-3390, 3314-3390 and 3316-3394 cm^{-1} in **Zn-H/NH$_2$·S**, **Zn-NO$_2$/NH$_2$·S** and **Zn-H/NO$_2$/NH$_2$·S**, respectively); *ii*) the complete ligand deprotonation (absence of the N-H stretching band typical of the pyrazole ring, falling at ν = 3175 cm^{-1})[26]; *iii*) the presence of clathrated DMF molecules (C=O stretching band in the range 1656-1667 cm^{-1}). The growth of the bands at ~1345 cm^{-1} upon passing from **Zn-H/NO$_2$·S** to Zn(BPZNO$_2$)·S and the bands in the range ~3315-3390 cm^{-1} upon passing from **Zn-H/NH$_2$·S** to Zn(BPZNH$_2$)·S (Figures 1b and S1b, respectively) is consistent with the increasing amount of the NO_2- and NH_2-functionalized ligands. In the MIXMOF **Zn-NO$_2$/NH$_2$·S**, the N-H stretching bands are very weak and rather broad if compared with those of the other compounds. This phenomenon cannot be ascribed to internal NH_2-NO_2 hydrogen bond interactions; in fact, as witnessed by ^{1}H MAS NMR (*vide infra*), hydrogen bonds are present in all MOFs containing the $BPZNH_2^{2-}$ ligand. The presence of a mixture of the Zn(BPZ)·S and Zn(BPZX)·S end members (X = NO_2, NH_2) in the four precipitates obtained could be ruled out in light of a number of experimental evidences.

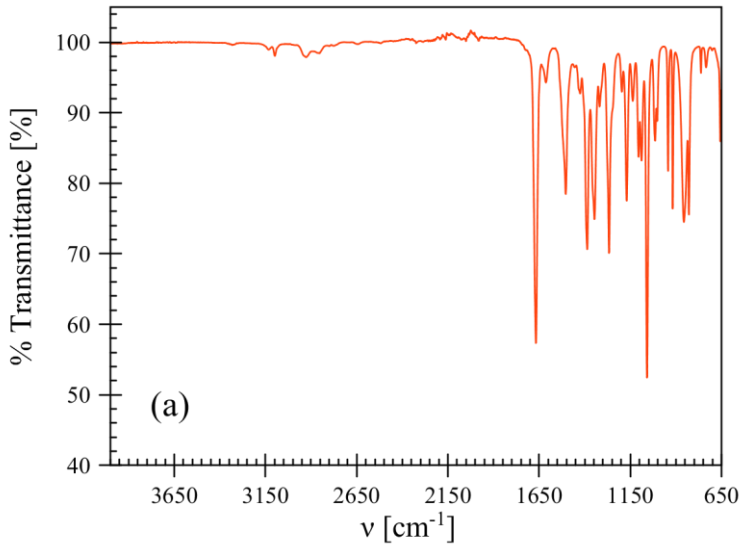

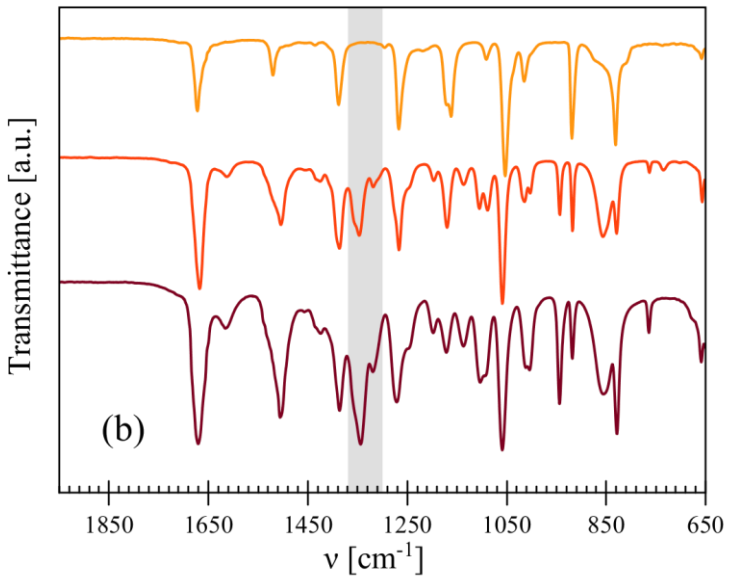

Figure 1. (a) Infrared spectrum of **Zn-H/NO₂·S**. (b) Magnification of the 1950-650 cm^{-1} range of the infrared spectra of Zn(BPZ)·S (orange trace), **Zn-H/NO₂·S** (red trace), and Zn(BPZNO₂)·S (dark red trace). The region of the symmetric NO stretching band is highlighted in grey.

Their PXRD patterns (Figure 2, Figures S4a-c) are clearly distinct from those of their single-ligand parents in terms of peak positions. In addition, as revealed by DSC, the decomposition process is characterized by a single peak (Table S1; Figure 3, Figures S5-S7).

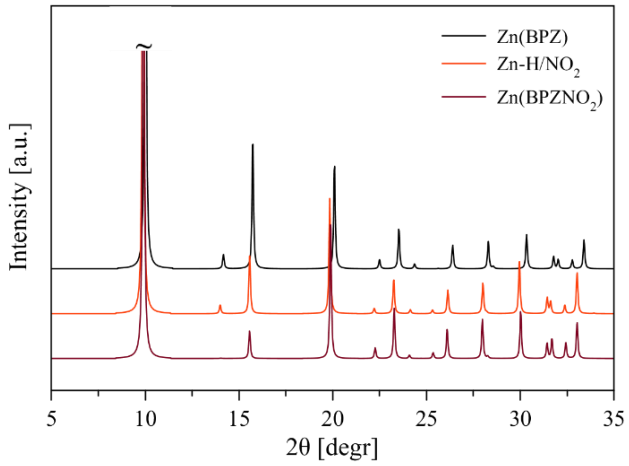

Figure 2. From top to bottom: low-angle region of the calculated PXRD patterns of Zn(BPZ), **Zn-H/NO₂** and Zn(BPZNO₂). Structural information for Zn(BPZ) and Zn(BPZNO₂) have been taken from references (14) and (12), respectively. Contents of ref. (12) reproduced with permission from John Wiley and Sons (Copyright 2018).

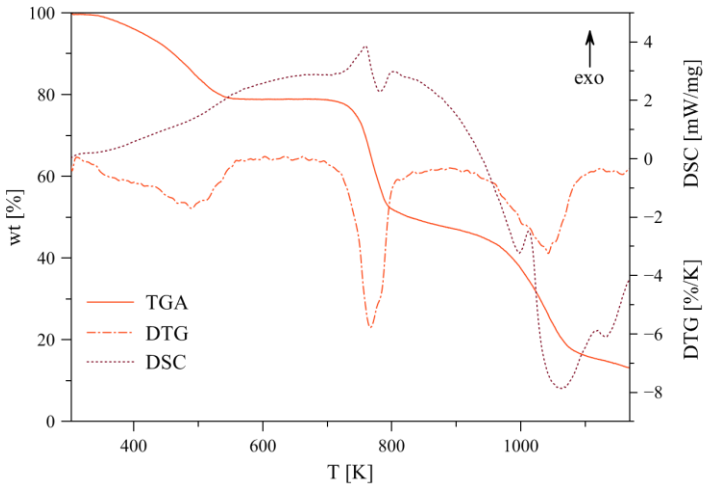

Figure 3. TGA (red continuous line), DTG (red dash-dotted line) and DSC (dark red dotted line) traces measured under a flow of N_2 on **Zn-H/NO$_2$·S**.

The accurate quantification of the ligand stoichiometric ratio in each MIXMOF was achieved through the combination of elemental analysis, crystal structure refinement and ^{13}C solid-state NMR spectroscopy.

(b) Solid-state ^{13}C and ^{15}N CPMAS NMR Analysis of the MIXMOFs and Quantification of the Linkers Stoichiometry. The accurate determination of the ligands composition in MIXMOFs is normally achieved through sample digestion in strongly acidic solutions (aqueous HCl, HF or H_2SO_4) followed by ^{1}H NMR analysis of the liquid mixture.[27] In our case this method is not informative, since the signals of the various ligands fall at nearly identical NMR chemical shifts in solution, preventing any assignment. Thus, the semi-quantitative solid-state NMR approach was exploited for the first time for ligands quantification in MIXMOFs. Direct solid-state NMR analysis of the as-synthesized materials avoids possible contaminations coming from the digestion procedure. In addition, NMR signal overlap in solution disappears in the solid state, as the resonances are much better resolved in the latter. Finally, as the ligands in the title MIXMOFs are almost identical, we can safely suppose nearly equal cross-polarization rates (*i.e.* T_{IS}) and ^{1}H $T_{1\rho}$ values, overcoming the quantitative limitations of the CPMAS experiment. The ^{13}C CPMAS NMR spectra of the end-members Zn(BPZ), Zn(BPZNO$_2$) and Zn(BPZNH$_2$) were collected and compared (Figure S8). The molecular structure with C atom numbering

of the BPZ^{2-} and $BPZX^{2-}$ ligands (X = NO_2, NH_2) is depicted in Scheme 2. The spectra exhibit distinctive features that are useful to identify each linker in the MOFs. In $BPZNO_2^{2-}$ and $BPZNH_2^{2-}$, the C3 atom bearing the $–NO_2$ or $–NH_2$ group is deshielded with respect to Zn(BPZ), falling at δ_C ~150 or ~152 ppm, respectively. The C3 and C3' signals show the same chemical shift (δ_C ~135 ppm) only in Zn(BPZ), where they are chemically and magnetically equivalent. $BPZNH_2^{2-}$ displays a characteristic resonance for C4 at δ_C ~99 ppm, while $BPZNO_2^{2-}$ and BPZ^{2-} feature signals at δ_C ~110 ppm ascribable to the C4 and C4' atoms, which are equivalent in BPZ^{2-}. The C5 and C5' signals show very close chemical shifts in all cases and are badly resolved. All the three MOFs contain a variable amount of DMF coming from the synthesis, as shown by the presence of signals at δ_C ~30 ppm (methyl groups) and 160 ppm (C=O group).

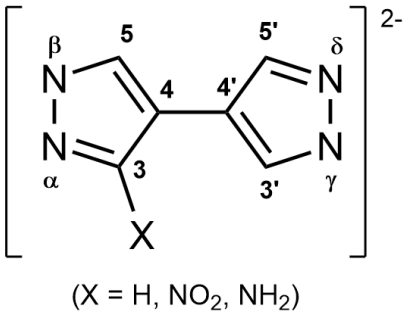

Scheme 2. C- and N-atom labelling of the $BPZX^{2-}$ ligands in the MOFs studied in this work.

The well-resolved resonances of the C4/C4' atoms in the $BPZNH_2^{2-}$ linker allowed for a quantitative estimation of the linkers composition in the MIXMOFs. Their ^{13}C CPMAS NMR spectra are shown in Figure 4, while Figure 5 illustrates the detailed integration and quantification procedure.

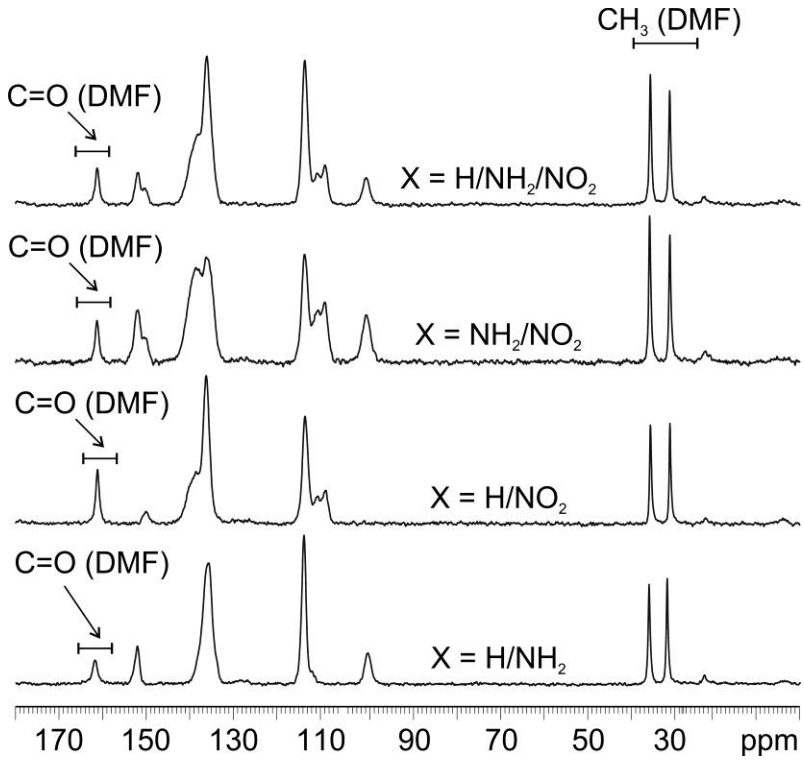

Figure 4. ^{13}C (150 MHz) CPMAS NMR spectra for **Zn-H/NH$_2$·S**, **Zn-H/NO$_2$·S**, **Zn-NO$_2$/NH$_2$·S** and **Zn-H/NO$_2$/NH$_2$·S** acquired at room temperature with a spinning speed of 20 kHz. The signals of DMF (synthesis solvent) are also highlighted for the sake of completeness. For the complete ^{13}C signals assignment refer to Figure S8 in the Supporting Information.

Deconvolution was adopted for overlapped resonances to discriminate the contribution of each signal of interest accurately in the experimental spectra (with the exception of **Zn-H/NH$_2$·S**, where the two diagnostic resonances are well resolved). The extrapolated integral values were used to calculate the relative amounts of each ligand in the solid phase, which were then converted into percentage values (Table 1; see Experimental Section for the methodology).

The approximate 50:50 ligand ratio is present only in **Zn-H/NH$_2$·S**, while the 64:36 [BPZ^{2-}: BPZNO$_2^{2}$] and 66:34 [BPZNH$_2^{2-}$: BPZNO$_2^{2-}$] ratios are found for **Zn-H/NO$_2$·S** and **Zn-NO$_2$/NH$_2$·S**, respectively. The triple-mixed MOF **Zn-H/NO$_2$/NH$_2$·S** shows a prevalence of the untagged ligand BPZ^{2-} (50%), while the remaining fraction is almost equally divided between the two tagged linkers BPZNH$_2^{2-}$ (23%) and BPZNO$_2^{2-}$ (27%).

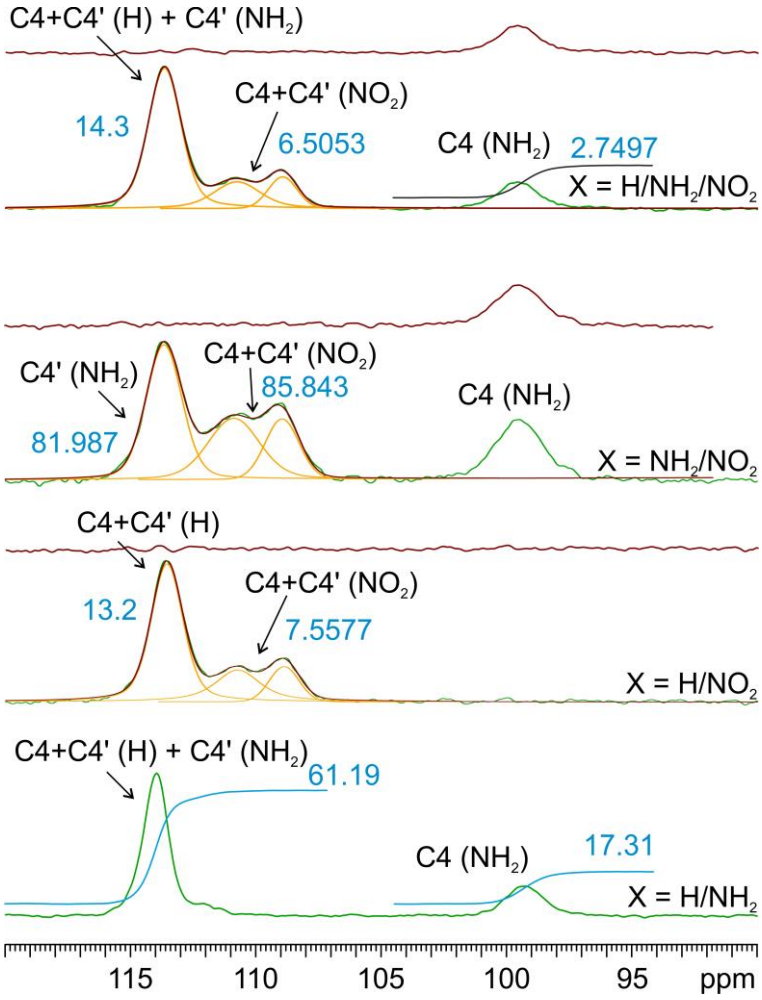

Figure 5. Magnification of the ^{13}C CPMAS NMR spectra of **Zn-H/NH₂·S**, **Zn-H/NO₂·S**, **Zn-NO₂/NH₂·S** and **Zn-H/NO₂/NH₂·S** in the 90-120 ppm δ region. Color code: experimental spectra, green; deconvolution of the signals between δ_C = 105 and 120 ppm, yellow; sum of the deconvoluted peaks, dark red; difference between the experimental spectra and the sum of the deconvoluted resonances, red line above. Integrals for the corresponding signals are written in blue.

Table 1. Relative percentage of the three ligands in the MIXMOFs reported in this study, as derived from the integration of the solid-state ^{13}C NMR spectra collected on the as-synthesized samples. In parenthesis, the values independently found by PXRD (see the Experimental Section).

Ligand	**Zn-H/NH₂**	**Zn-H/NO₂**	**Zn-NO₂/NH₂**	**Zn-H/NO₂/NH₂**
BPZ^{2-}	55.9 (56)	63.6 (62)	-	49.1 (46)
$BPZNH_2^{2-}$	44.1 (44)	-	65.6 (62)	23.3 (21)

$BPZNO_2^{2-}$	-	36.4 (38)	34.4 (38)	27.6 (33)

The ^{15}N CPMAS NMR spectra of the end-members and MIXMOFs studied in this work are collected in Figures S9 and 6, respectively. From a comparison of these spectra, it can be inferred that the signals of all the pyrazole N atoms, apart from that closer to the substituent X (Nα, Scheme 2), fall at δ_N ~250 ppm. At variance, the position of Nα depends on the nature of X: it is coincident to that of Nβ–δ for X = H (all the nitrogen atoms are magnetically and chemically equivalent in BPZ^{2-}), while it falls at δ_N ~200 and 220 ppm for X = NO_2 and NH_2, respectively. The signals of the amino and nitro groups are found at δ_N ~30 and 360 ppm, respectively. The signal of the nitro group is very broad (as already observed in the literature)[28] and visible only for Zn($BPZNO_2$), where $BPZNO_2^{2-}$ is not diluted by the other ligands. The nitrogen atom of the DMF solvent used for the syntheses is observed as a singlet at δ_N ~100 ppm. Unfortunately, all the spectra are characterized by a very low signal-to-noise ratio and are badly resolved to allow for a stoichiometric quantification. Therefore, we referred to the ^{13}C data only to assess the real samples unit formulae.

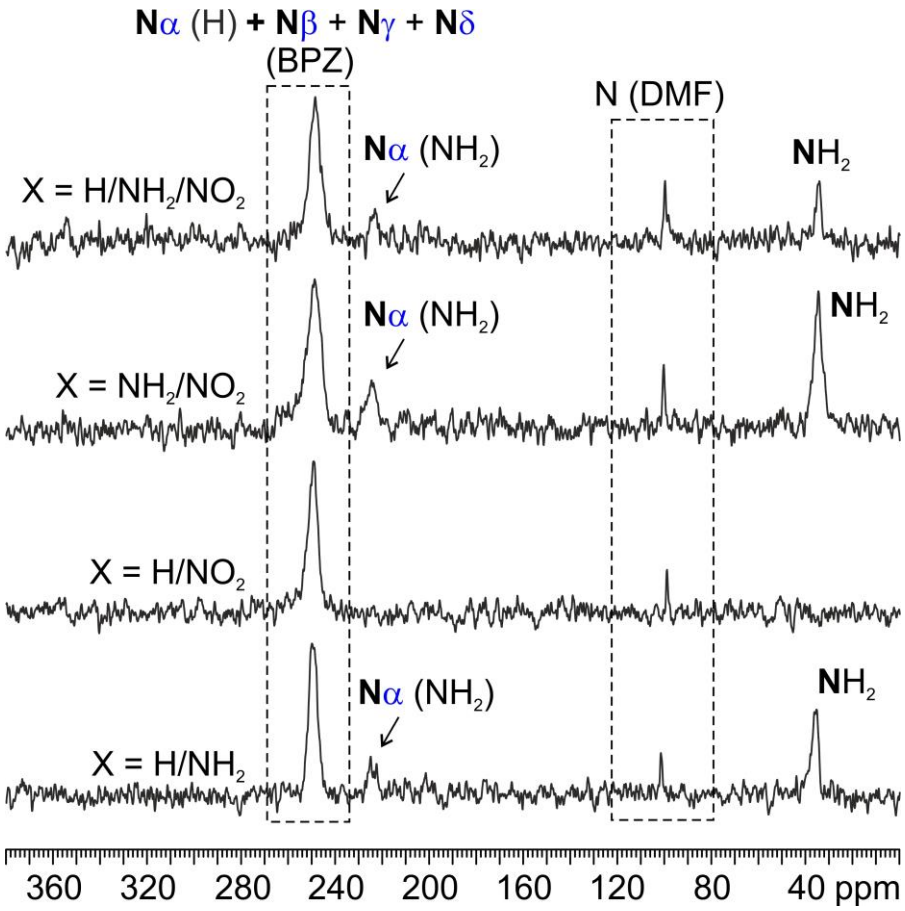

Figure 6. ^{15}N (60 MHz) CPMAS NMR spectra of **Zn-H/NH$_2$·S**, **Zn-H/NO$_2$·S**, **Zn-NO$_2$/NH$_2$·S** and **Zn-H/NO$_2$/NH$_2$·S** acquired at room temperature with a spinning speed of 12 kHz. The ^{15}N peak related to DMF is observed in all samples and assigned at δ_N ~100 ppm.

In the crystal structure, the ligands occupy a (2/*m*) special position, which implies that the NO_2 or NH_2 substituents are disordered on the four skeletal carbon atoms (see the Experimental Section for further details). This occurrence prevents the unambiguous assessment of the real tag position on the ligand, as well as its relative location with respect to the nearby ligands in the framework. Hence, the presence of hydrogen bonds cannot be confirmed or excluded by PXRD alone. ^{1}H MAS NMR spectra were then acquired to evaluate the presence of hydrogen bonds in the end-members, as well as in the MIXMOFs. Indeed, the appearance of protonic resonances at chemical shift values higher than 10 ppm is usually associated to ^{1}H nuclei involved in hydrogen bond interactions.[29] Figures S10-S12 show the spectra of the end-members and of the MIXMOFs. In the spectrum of Zn(BPZNH$_2$), a resonance ascribable to the hydrogen-bonded protons of the amino group is visible at δ_H = 10.3 ppm (Figure S11). On the contrary,

no such signal is detectable in the spectra of either Zn(BPZ) or Zn($BPZNO_2$). As for the MIXMOFs, a broad and very low-intensity shoulder is visible in the spectra of all samples containing $BPZNH_2^{2-}$ at δ_H ~10 ppm (Figure S12). This is due to the presence of residual hydrogen bonds of the amino groups. The intensity of this signal is roughly proportional to the dilution of the NH_2 tag in the MIXMOF.

(c) Crystal Structure Analysis. The four MIXMOFs show the same structural motif of the end members Zn(BPZ),[14] Zn($BPZNO_2$)[12] and Zn($BPZNH_2$),[13] which, for the sake of completeness, will be briefly described in the following. **Zn-H/NO_2·S** and **Zn-H/NH_2·S** crystallize in the tetragonal space group $P4_2/mmc$. Tetrahedral MN_4 nodes (Figures 7a and S13a) and *exo*-tetradentate spacers define a 3-D (4,4)-connected porous network (Figures 7b and S13b), in which 1-D square channels run parallel to the [001] crystallographic direction. The analysis of the crystal lattice from a topological point of view through the software TOPOS 4.0[30] and considering both Zn(II) and the 4,4′-bipyrazolates as tetra-connected nodes led to the assignment of the network topology symbol ($3^{12} \cdot 4^{24} \cdot 5^9$), belonging to the **10-c** net. **Zn-NO_2/NH_2·S** and **Zn-H/NO_2/NH_2·S** show the lower orthorhombic symmetry (space group *Cccm*, proper subgroup of $P4_2/mmc$), implying rhombic 1-D channels (Figure S14). The topological analysis of the crystal lattice revealed the same topology as above. The torsion angle of the NO_2 group with respect to the 4,4′-bis(pyrazolate) plane passes from nearly zero (in **Zn-H/NO_2·S**) to ~81° and 128° in **Zn-NO_2/NH_2·S** and **Zn-H/NO_2/NH_2·S**, respectively.

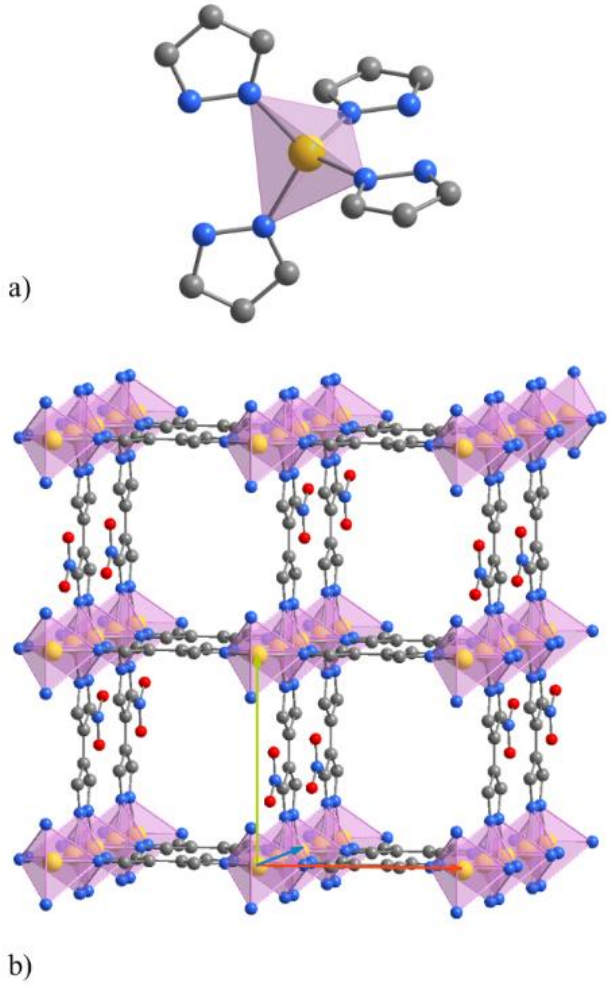

Figure 7. Representation of the crystal structure of **Zn-H/NO_2·S**: (a) the tetrahedral node. (b) Portion of the crystal packing viewed along the [115] crystallographic direction. Unit cell axes: *a* (red); *b* (green) and *c* (blue). Carbon, grey; nitrogen, blue; oxygen, red; zinc, yellow. The hydrogen atoms and solvent molecules have been omitted for the sake of clarity. An ordered model has been adopted in the picture preparation for the position of the NO_2 groups on the ligand skeleton. Main bond distances and angles: Zn-N, 2.018(9) Å; Zn···Zn, 3.6833(2), 8.9394(4) Å; N-Zn-N, 109.16(14)-110.1(3)°.

At room temperature and pressure conditions, the empty volume[31] ranges from ~41% in **Zn-NO_2/NH_2** up to ~47% in **Zn-H/NO_2/NH_2** [see Table 2 for the value of the four compounds and the end-members Zn(BPZ), Zn($BPZNO_2$) and Zn($BPZNH_2$)]. This means a pore volume[32] *per* cell ranging from ~0.33 to ~0.39 $cm^3\,g^{-1}$ (Table 2). In all the MIXMOFs, DMF was found disordered within the channels.

Table 2. Comparison of the empty volume[31,32] of **Zn-H/NO_2**, **Zn-H/NH_2**, **Zn-NO_2/NH_2** and **Zn-H/NO_2/NH_2** with respect to the end-members Zn(BPZ), Zn($BPZNO_2$) and Zn($BPZNH_2$). In parenthesis, the empty volume calculated assuming that the nitro groups are coplanar to the 4,4'-bis(pyrazolate) skeleton.

Compound	Empty volume [%]	Empty volume [cm^3/g]
Zn-H/NO_2	46(46)	0.37(0.37)
Zn-H/NH_2	42	0.36
Zn-NO_2/NH_2	42(45)	0.33(0.35)
Zn-H/NO_2/NH_2	44(46)-46(47)[31]	0.36(0.37)-0.38(0.39)[31]
Zn(BPZ)[14]	42	0.37
Zn($BPZNO_2$)[12]	39(40)	0.29(0.29)
Zn($BPZNH_2$)[13]	46	0.38

PXRD alone cannot assess whether the ligands in the four MIXMOFs show a random, alternating or cluster distribution.[7a, 33] Nonetheless, after thermal activation, we verified that the unit cell parameters of the two series Zn(BPZ), **Zn-H/NO_2** and Zn($BPZNO_2$), and Zn(BPZ), **Zn-H/NH_2** and Zn($BPZNH_2$) approximately follow the Vegard Law.[34] Upon increasing the amount of tagged ligand, the *c*-axis lengthens while the *a*- and *b*-axis shrink, with an overall volume shrinkage of ~2.5 and 4.1%, respectively (Figures 8 and S15). Though apparently counterintuitive, the unit cell volume reduction with the increase of the amount of tagged ligand in the MIXMOF has been previously observed, e.g. for (MIX)MOF-5[35] and (MIX)UiO-66,[36] bearing the terephtalate/2-amino-terephtalate linker couple. The observed increase of the *c*-axis in the title compounds is possibly due to an increased steric hindrance along the [001] crystallographic direction caused by the dangling tags. Consequently, the *a*- and *b*-axes shrink to preserve the integrity of the Zn-N coordinative bonds, as confirmed by the correlation observed between the *a*- and *c*-axis (*a*/*c*) and the ligand stoichiometric ratio (Figures 8 and S15).

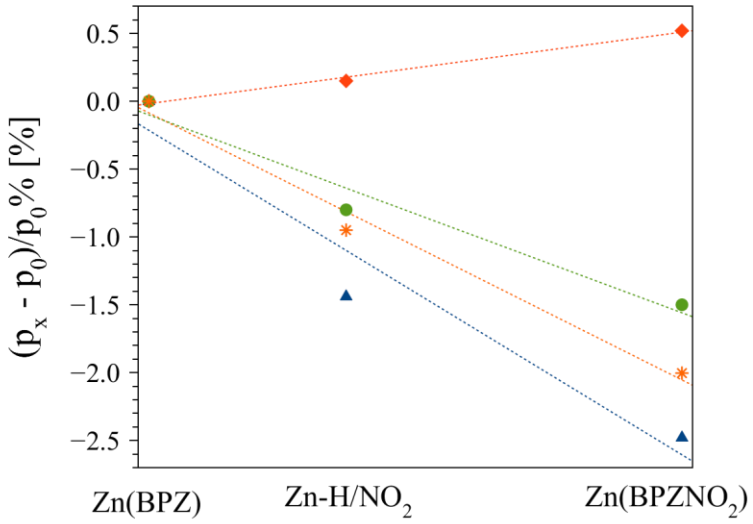

Figure 8. Percentage variation of the unit cell parameters (p_X) of Zn(BPZ), **Zn-H/NO$_2$**, and Zn(BPZNO$_2$) as a function of the ligand stoichiometric ratio. The values reported for each compound have been normalized with respect to those of Zn(BPZ). Structural parameters: *a* (green circles), *c* (red diamonds), *V* (blue triangles) and *a*/*c* (orange stars).

The MIXMOFs **Zn-NO$_2$/NH$_2$** and **Zn-H/NO$_2$/NH$_2$** have a crystallographic symmetry different from their end-members. Therefore, a direct correlation of the unit cell parameters cannot be made, except for the *c*-axis (running parallel to the metal ion chains). In order to overcome this issue, we have compared (Figure S16) the distance between consecutive metal ions along the 1-D chains (d_{Zn}, Figure S17) and between two Zn(II) ions belonging to nearby chains and bridged by a ligand (D_{Zn}, Figure S17). Both parameters reveal a trend similar to that of **Zn-H/NO$_2$** and **Zn-H/NH$_2$**: an overall shrinkage of the unit cell volume and the growth of the *c*-axis passing from the untagged to the tagged compounds.

(d) Thermal Behaviour. The four MIXMOFs show a high thermal stability, with decomposition temperatures in the range 708-726 K under N_2 (see Table S1 and Figures 3 and S5-S7 for details). As expected, the decomposition temperature of the MIXMOFs is influenced by the presence of the nitro group: the higher the amount of $BPZNO_2^{2-}$, the lower the thermal stability.[12, 37] Indeed, T_{dec} follows the trend: **Zn-H/NH$_2$** > **Zn-H/NO$_2$/NH$_2$** > **Zn-NO$_2$/NH$_2$** > **Zn-H/NO$_2$**. Considering the destabilizing effect of the electron-withdrawing group NO_2, this behaviour may be associated with the presence of weaker

M-N bonds. The initial weight loss showed in all the thermogravimetric traces (Figures 3 and S5-S7) corresponds to the loss of the solvent trapped in the channels. After desolvation, the materials are stable up to decomposition. *In situ* variable-temperature powder X-ray diffraction experiments followed by a parametric Le Bail refinement were performed on all compounds (Figures 9 and S18-S21). Table S2 collects the main structural data concerning the PXRD thermal characterization of the four MIXMOFs. **Zn-H/NH_2·S**, **Zn-NO_2/NH_2·S** and **Zn-H/NO_2/NH_2·S** do not show any phase transition or loss of crystallinity upon heating. The progressive shortening of the unit cell axes lengths (*a* and *c* for **Zn-H/NH_2·S** and **Zn-NO_2/NH_2·S**; *b* and *c* for **Zn-H/NO_2/NH_2·S**) leads to a volume shrinkage in the range ~0.6-1.4%. On the contrary, **Zn-H/NO_2·S** shows several phase transitions during solvent loss, passing from the original tetragonal symmetry ($P4_2/mmc$) of the solvated phase to orthorhombic (*Cccm*, proper subgroup of $P4_2/mmc$), monoclinic (*C2/c*, proper subgroup of *Cccm*) and orthorhombic again (*Cccm*), before transforming into a tetragonal desolvated form with the same space group of the initial phase (Figure 9). The four phases have the same structural motif, hence **Zn-H/NO_2** does not lose its pristine porosity. As found in the other MIXMOFs, a volume contraction of ~1% due to the decrease of the *a*- and *c*-axes (by ~-0.3% and ~-0.5%, respectively) is observed before decomposition (Figure 10).

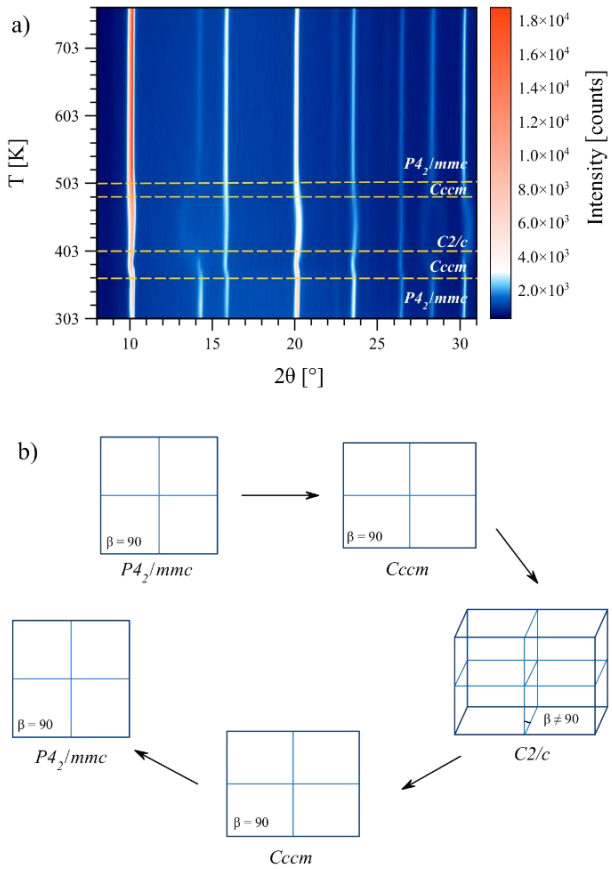

Figure 9. (a) 2-D plot of the powder X-ray diffraction patterns measured on **Zn-H/NO₂·S** as a function of temperature heating in air, with steps of 20 K, up to 763 K. (b) Scheme of the phase transitions undergone by **Zn-H/NO₂·S** during the desolvation process (T = 363-503 K).

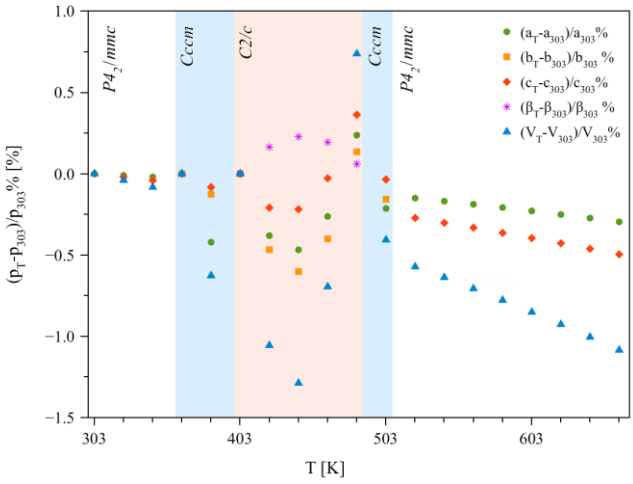

Figure 10. Percentage variation of the unit cell parameters (p_T) of **Zn-H/NO₂·S** as a function of temperature. At each temperature, the reported values have been normalized with respect to those at which the specific crystal phase was first

observed ($P4_2/mmc$: T_0 = 303 K, *Cccm*: T_0 = 363 K, *C2/c*: T_0 = 403 K). *a*, green circles; *b*, yellow squares; *c*, red diamonds; *β*, pink stars; *V*, blue triangles.

(e) Textural properties and CO_2 adsorption ability across the MIXMOF family. The textural properties of the title MOFs were studied by means of N_2 adsorption at 77 K after thermal activation (393 K, 10^{-6} Torr, 24 h). To verify the activation completion, we carried out a thermogravimetric analysis on all the activated samples: the absence of weight loss before decomposition (Figure S22) proves that a complete activation has been obtained. Table 3 collects the main textural properties of the four MIXMOFs. As shown in Figure 11, **Zn-H/NO_2**, **Zn-NO_2/NH_2** and **Zn-H/NO_2/NH_2** possess a type I isotherm typical of microporous solids, while **Zn-H/NH_2** is featured by a type IV isotherm, typical of a micro-mesoporous substance. The BET areas fall in the 400-600 m^2/g range. The areas are slightly smaller than those measured for Zn(BPZ) (930 m^2/g)[14] and slightly higher than those of Zn($BPZNH_2$) (395 m^2/g),[13] in line with the "density" of dangling tags present in the pores (the higher the amount of tags, the lower the surface area available).[38] All N_2 isotherms show narrow hysteresis loops in the high p/p_0 region. Steep uptake at pressures close to condensation is ascribed to the presence of macropores between MOF crystallites. This is confirmed by the SEM images of selected samples, showing the presence of macroscopic cavities around 200 nm for **Zn-NO_2/NH_2** (Figure 12a-b) and in the 50-70 nm size range for **Zn-H/NO_2/NH_2** (Figure 12c-d). The Dubinin-Astakhov analysis also revealed that the micropore volume represents the main contribution to the total pore volume for all samples (with the exception of **Zn-H/NH_2**).

Table 3. Textural parameters of the four MIXMOFs reported in this study, as derived from their N_2 adsorption isotherms at 77 K.

Compound	SSA BET [m^2/g]	V_{micro} (% of V_{tot}) [cm^3/g]	V_{tot} [cm^3/g]
Zn-H/NO_2	431	0.27 (79%)	0.34
Zn-H/NH_2	502	0.21 (32%)	0.66
Zn-NO_2/NH_2	567	0.23 (70%)	0.33
Zn-H/NO_2/NH_2	588	0.23 (70%)	0.33

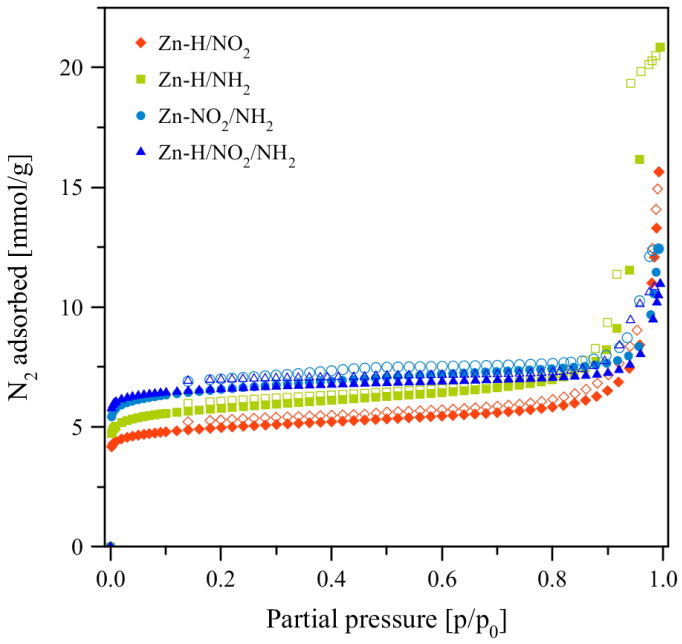

Figure 11. N_2 adsorption isotherms measured at 77 K on **Zn-H/NO_2** (red diamonds), **Zn-H/NH_2** (light green squares), **Zn-NO_2/NH_2** (cyan circles) and **Zn-H/NO_2/NH_2** (blue triangles). Empty symbols denote desorption branches.

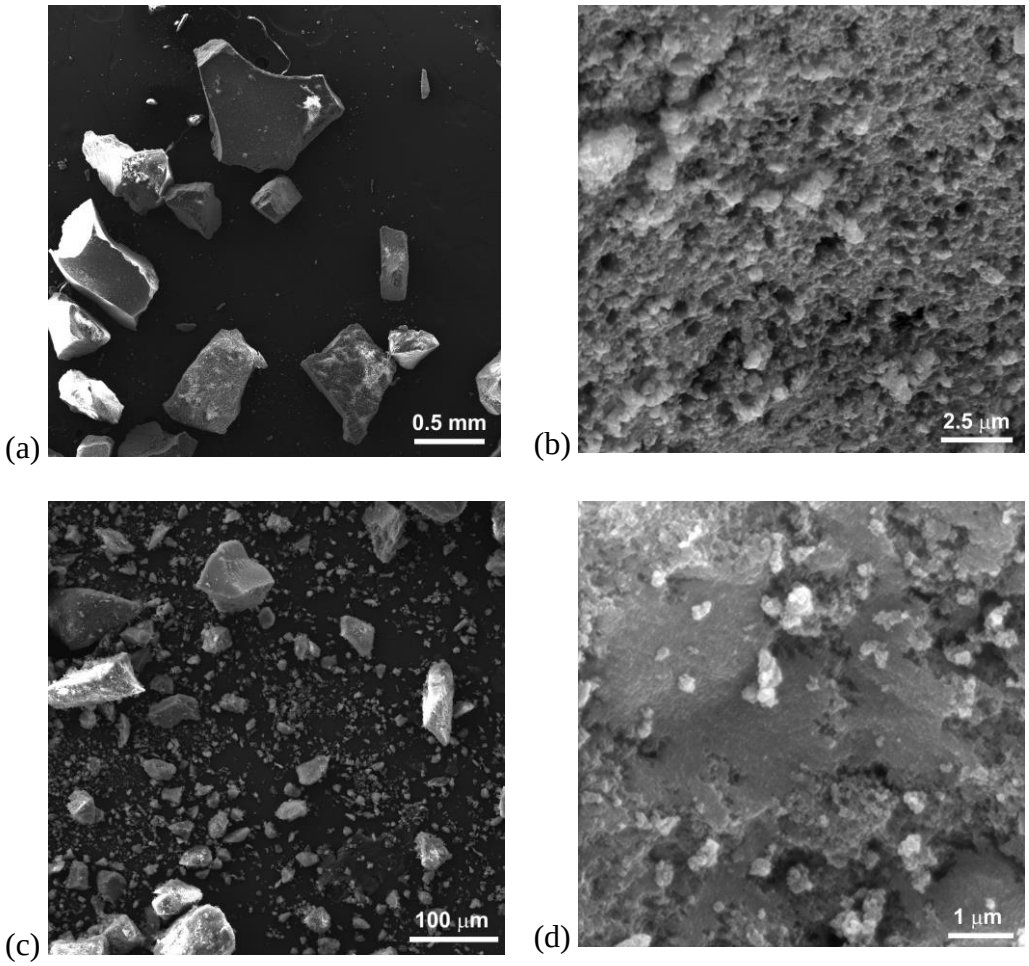

Figure 12. SEM images of **Zn-NO_2/NH_2** (a-b) and **Zn-H/NO_2/NH_2** (c-d). The presence of macropores between the crystallites is clearly visible in both samples.

The MIXMOF samples have been tested as CO_2 adsorbents at ambient temperature and pressure conditions. To assess the samples thermodynamic stability in humid conditions (typical of many industrial processes dealing with gas mixtures separation), their PXRD profiles were collected at regular time intervals after exposure to a water vapor saturated atmosphere. As shown in Figure S23, all the MIXMOFs are stable in the conditions we adopted for at least 11 days. To establish an experimental correlation between MIXMOF composition and carbon dioxide uptake capacity, their CO_2 adsorption isotherms (Figure 13) have been collected. In addition, the Henry and IAST CO_2/N_2 selectivity and CO_2 isosteric heat of adsorption (Q_{st}) have been evaluated. The results have been compared with those of their end-parents Zn(BPZ)/Zn(BPZX) (X = NO_2, NH_2) and with other zinc(II) single-azolate-ligand MOFs from

the literature where similar measurements have been carried out.[10a, 39] The whole dataset is reported in Table 4. The best-performing samples of the family are those bearing amino groups as tags. The strong affinity of the (acidic) carbon dioxide for basic groups is well-documented in the literature, including examples of NH_2-tagged azolate MOFs used for this purpose.[10a, 40] This is also mirrored by the high Q_{st} values recorded for **Zn-H/NH2** (30.8 kJ mol^{-1}) and Zn($BPZNH_2$) (35.6 kJ mol^{-1}),[13] if compared with that of Zn(BPZ) (22.0 kJ mol^{-1}). On the contrary, the introduction of a nitro tag is not beneficial to improve the thermodynamic affinity for CO_2. Indeed, **Zn-H/NO2** and Zn($BPZNO_2$) are featured by lower Q_{st} values (21.6 and 20.5 kJ mol^{-1}, respectively). In **Zn-NO2/NH2** and **Zn-H/NO2/NH2**, the simultaneous presence of nitro and amino substituents within the same MOF drastically reduces Q_{st} and the amount of CO_2 adsorbed with respect to **Zn-H/NO2**, **Zn-H/NH2**, Zn($BPZNO_2$) and Zn($BPZNH_2$), despite their comparable surface areas. An identical conclusion can be drawn for the triple-mixed MOF **Zn-H/NO2/NH2**, where there is no substantial improvement in the introduction of BPZ^{2-} to "dilute" the two tags in the solid phase. Interestingly, the CO_2/N_2 selectivity improves when tags are more "diluted" in the sample. Indeed, **Zn-H/NO2** shows a better selectivity than Zn($BPZNO_2$), and the same occurs for **Zn-H/NH2** when compared with Zn($BPZNH_2$). From all these considerations, we can conclude that the MIXMOF **Zn-H/NH2** is the best compromise between surface area, CO_2 uptake, Q_{st} value and CO_2/N_2 selectivity among all the MIXMOFs taken into account in this study. In comparison with other azolate-containing Zn(II) MOFs from the literature, our MIXMOFs show a better performance, in terms of both CO_2 affinity (Q_{st}) and adsorption capacity (mmol/g), than other literature samples featured by higher BET areas like their methylated counterpart Zn(Me_2BPZ)[39a] or the Zn(BDP-X) family.[10a]

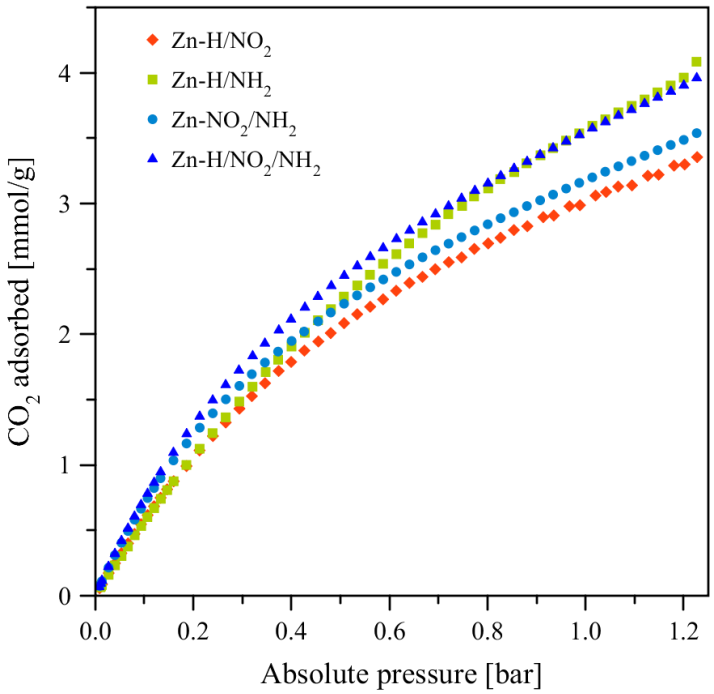

Figure 13. CO_2 adsorption isotherms measured at 298 K on **Zn-H/NO2** (red diamonds), **Zn-H/NH2** (light green squares), **Zn-NO2/NH2** (cyan circles) and **Zn-H/NO2/NH2** (blue triangles).

Table 4. Comparison of the CO_2 adsorption properties of the MIXMOFs examined in this study and with selected zinc(II) azolate MOFs from the literature. Data were extrapolated from the presented graphs when not directly available in the article discussion. H_2BDP = 1,4-bis(1*H*-pyrazol-4-yl)benzene; H_2BDP-NO_2 = 2-nitro[1,4-bis(1*H*-pyrazol-4-yl)benzene]; H_2BDP-NH_2 = 2-amino[1,4-bis(1*H*-pyrazol-4-yl)benzene]; H_2BDP-OH = 2-hydroxo[1,4-bis(1*H*-pyrazol-4-yl)benzene]; pyz = pyrazine; H_2(Me_2BPZ) = 3,3′-dimethyl-1*H*,1′*H*-4,4′-bipyrazole.

	BET area [m^2/g]	**Q_{st}** [kJ mol^{-1}]	**CO_2/N_2 selectivity (Henry)**	**CO_2/N_2 selectivity (IAST)**	**CO_2 quantity adsorbed (p = 1 bar) [mmol/g]** T = 298 K	T = 273 K	**Quantity adsorbed @ 298K/SSA** [mmol/m^2]	**Reference**
Zn(BPZ)	930	22.0	15	15	3.7 (16.2 wt.%)	5.1 (22.5 wt.%)	0.0040	This work and 39a
Zn(BPZNO_2)	916	20.5	15	12	4.4 (19.2 wt.%)	4.7 (20.6 wt.%)	0.0048	12
Zn(BPZNH_2)	395	35.6	17	14	3.1 (13.5 wt.%)	4.8 (20.9 wt.%)	0.0078	13
Zn-H/NH_2	502	30.8	18	17	3.6 (15.8 wt.%)	5.1 (22.3 wt.%)	0.0072	This work
Zn-H/NO_2	431	21.6	20	20	3.0 [41] (13.3 wt.%)	2.4 (10.6 wt.%)	0.0070	This work
Zn-NO_2/NH_2	567	19.0	14	12	3.2 (14.0 wt.%)	3.3 (14.4 wt.%)	0.0056	This work
Zn-H/NO_2/NH_2	588	16.1	11	11	3.6 (15.7 wt.%)	4.1 (17.9 wt.%)	0.0061	This work

Zn(BDP)	2288	19.7			~ 3.0		10a
Zn(BDP-NO_2)	1875	21.4			~ 2.9		10a
Zn(BDP-NH_2)	1345	28.1			~ 2.8		10a
Zn(BDP-OH)	1170	22.9			~ 4.5		10a
$[Zn(SiF_6)(pyz)_2]_n$ (SIFSIX-3-Zn)	250	45.0	1818	2.5		0.0100	39b
Zn(Me_2BPZ)	290	24.8			2.0		39a

Conclusions

A series of mixed-ligand Zn(II) MOFs containing 4,4'-bipyrazolate spacers bearing different chemical tags has been prepared and fully characterized. The described compounds are the first examples of *(pyr)azolate-based* MIXMOFs, in contrast to a large number of existing carboxylate-based analogues. The determination of the exact ligand stoichiometric composition within MIXMOF phases is normally achieved through sample destruction in strong acids or bases followed by ^{1}H NMR analysis of the digested sample. When the linkers are structurally very similar (as in this case), solution NMR signal integration needed for quantification is hampered by strong peaks overlapping. To solve this problem, *solid state* ^{13}C NMR spectroscopy has been exploited instead in this work for the first time, achieving a far better signal resolution.

The systematic experimental study carried out on samples built with all the BPZ^{2-} and $BPZX^{2-}$ (X = NH_2, NO_2) linkers combinations conceivable has unveiled an interesting relationship between MIXMOF composition and CO_2 uptake capacity for Carbon Capture and Sequestration (CCS) applications. The introduction of chemical tags of different nature generally improves the adsorption capacity (in terms of mmol/g adsorbed) if compared with the parent untagged Zn(BPZ) compound, providing experimental evidence for the computational studies of the recent literature.[8b] Furthermore, the presence of the amino tag strongly enhances both the amount of CO_2 adsorbed and the CO_2 thermodynamic affinity (Q_{st}), while the opposite occurs for the nitro substituent. The simultaneous presence of nitro and amino functions within the same solid phase is not beneficial for gas uptake. Finally, to improve the CO_2 selectivity over N_2, it is important to reduce tags concentration in the solid phase [*i.e.* **Zn-H/NO$_2$** *vs.* Zn($BPZNO_2$) or **Zn-H/NH$_2$** *vs.* Zn($BPZNH_2$)]. Taking all these considerations into account, the best combination resulted in the mixed-ligand MOF **Zn-H/NH$_2$**.

Conflicts of Interest. The authors have no conflicts of interest to declare.

Associated Content

Supporting Information. IR spectra of **Zn-H/NH_2·S**, **Zn-NO_2/NH_2·S** and **Zn-H/NO_2/NH_2·S** (Figures S1-S2). Graphical result of the final Rietveld refinements for **Zn-H/NH_2**, **Zn-NO_2/NH_2**, **Zn-H/NO_2/NH_2** and **Zn-H/NO_2** (Figure S3). Comparison of the PXRD patterns of **Zn-H/NH_2**, **Zn-NO_2/NH_2** and **Zn-H/NO_2/NH_2** with those of the end members (Figure S4). TGA and DSC traces of **Zn-H/NH_2·S**, **Zn-NO_2/NH_2·S** and **Zn-H/NO_2/NH_2·S** (Figures S5-S7). Decomposition temperatures of the four MIXMOFs (Table S1). ^{13}C and ^{15}N CPMAS NMR spectra of the single-linker MOFs Zn(BPZ), Zn($BPZNH_2$) and Zn($BPZNO_2$) (Figures S8-S9). ^{1}H MAS NMR spectra of single-ligand and mixed ligands MOFs (Figures S10-S12). Representation of the crystal structure of **Zn-H/NH_2·S** and **Zn-NO_2/NH_2·S** (Figures S13-S14). Vegard law plots of **Zn-H/NH_2**, **Zn-NO_2/NH_2**, **Zn-H/NO_2/NH_2** (Figures S15-S17). VT-PXRD patterns of **Zn-H/NO_2·S**, **Zn-H/NH_2·S** and **Zn-NO_2/NH_2·S** and **Zn-H/NO_2/NH_2·S** (Figures S18-S21). TG profiles of the MIXMOFs after thermal activation (Figure S22). PXRD patterns of the MIXMOFs exposed to a water vapor saturated atmosphere over 11 days (Figure S23). Percentage variation of the unit cell parameters of the four MIXMOFs as a function of the temperature (Table S2).

Author Information

Corresponding Authors

* Prof. Simona Galli. E-mail: simona.galli@uninsubria.it

* Dr. Andrea Rossin. E-mail: andrea.rossin@iccom.cnr.it

ORCID

Andrea Rossin: 0000-0002-1283-2803

Simona Galli: 0000-0003-0335-5707

Michele Chierotti: 0000-0002-8734-6009

Giuliano Giambastiani: 0000-0002-0315-3286

Claudio Pettinari: 0000-0002-2547-7206

Giulia Tuci: 0000-0002-3411-989X

Rebecca Vismara: 0000-0001-9474-7671

Acknowledgments

S.G. and R.V. acknowledge Università dell'Insubria for partial funding. G.T. and G.G. thank the Italian MIUR through the PRIN 2015 Project SMARTNESS (2015K7FZLH) for financial support. G.G. thanks the TRAINER project (Catalysts for Transition to Renewable Energy Future) Ref. ANR-17-MPGA-0017 for support. C.P. thanks the University of Camerino and the Italian MIUR throughout the PRIN 2015 Project Towards a Sustainable Chemistry (20154X9ATP_002). The authors thank the Italian National Research Council (CNR) microscopy facility "Ce.M.E.–Centro Microscopie Elettroniche Laura Bonzi" for providing the SEM facilities acquired through the "Ente Cassa di Risparmio di Firenze" Grant Number n.2013.0878 and Regione Toscana POR FESR 2014-2020 for the project FELIX (Fotonica ed Elettronica Integrate per l'Industria), Grant Number 6455.

References

1. (a) *Metal-Organic Frameworks: Applications in Separations and Catalysis*. Wiley-VCH: 2018(b) *The Chemistry of Metal-Organic Frameworks: Synthesis, Characterization, and Applications*. Wiley-VCH: 2016(c) Seyyedi, B., *Metal-Organic Frameworks: a New Class of Crystalline Porous Materials*. Lambert Academic Publishing: Saarbrücken: 2014(d) MacGillivray, L. R.; Lukehart, C. M., *Metal-Organic Framework Materials*. John Wiley & Sons: New York: 2014.
2. (a) Rossin, A.; Tuci, G.; Luconi, L.; Giambastiani, G., Metal–Organic Frameworks as Heterogeneous Catalysts in Hydrogen Production from Lightweight Inorganic Hydrides. *ACS Catal.* **2017,** *7*, 5035–5045. (b) Yi, F.-Y.; Chen, D.; Wu, M.-K.; Han, L.; Jiang, H.-L., Chemical Sensors Based on Metal–Organic Frameworks. *ChemPlusChem* **2016,** *81*, 675-690. (c) Chughtai, A. H.; Ahmad, N.; Younus, H. A.; Laypkovc, A.; Verpoort, F., Metal–Organic Frameworks: Versatile Heterogeneous Catalysts for Efficient Catalytic Organic Transformations. *Chem. Soc. Rev.* **2015,** *44*, 6804-6849. (d) Liu, J.;

Chen, L.; Cui, H.; Zhang, J.; Zhang, L.; Su, C.-Y., Applications of Metal–Organic Frameworks in Heterogeneous Supramolecular Catalysis. *Chem. Soc. Rev.* **2014,** *43*, 6011-6061. (e) Hu, Z.; Deibert, B. J.; Jing, L., Luminescent Metal–Organic Frameworks for Chemical Sensing and Explosive Detection. *Chem. Soc. Rev.* **2014,** *43*, 5815-5840. (f) Gascon, J.; Corma, A.; Kapteijn, F.; Llabrés i Xamena, F. X., Metal Organic Framework Catalysis: *Quo Vadis*? *ACS Catal.* **2014,** *4*, 361–378. (g) Suh, M. P.; Park, H. J.; Prasad, T. K.; Lim, D. W., Hydrogen Storage in Metal–Organic Frameworks. *Chem. Rev.* **2012,** *112*, 782-835. (h) Horcajada, P.; Serre, C.; Maurin, G.; Ramsahye, N. A.; Balas, F.; Vallet-Regi, M.; Sebban, M.; Taulelle, F.; Férey, G., Flexible Porous Metal-Organic Frameworks for a Controlled Drug Delivery. *J. Am. Chem. Soc.* **2008,** *130*, 6774–6780.

3. *Metal-Organic Frameworks (MOFs) for Environmental Applications*. Elsevier (Amsterdam): 2019.
4. (a) Song, C.; Hu, J.; Ling, Y.; Feng, Y.; Krishna, R.; Chen, D.; He, Y., The Accessibility of Nitrogen Sites Makes a Difference in Selective CO_2 Adsorption of a Family of Isostructural Metal–Organic Frameworks. *J. Mater. Chem. A* **2015,** *3*, 19417-19426. (b) Zhang, Z.; Yao, Z.-Z.; Xiang, S.; Chen, B., Perspective of Microporous Metal-Organic Frameworks for CO_2 Capture and Separation. *Energy Environ. Sci.* **2014,** *7*, 2868-2899. (c) Song, C.; He, Y.; Li, B.; Ling, Y.; Wang, H.; Feng, Y.; Krishna, R.; Chen, B., Enhanced CO_2 Sorption and Selectivity by Functionalization of a NbO-Type Metal–Organic Framework with Polarized Benzothiadiazole Moieties. *Chem. Commun.* **2014,** *50*, 12105-12108.
5. (a) Jiao, J.; Gong, W.; Wu, X.; Yang, S.; Cui, Y., Multivariate Crystalline Porous Materials: Synthesis, Property and Potential Application. *Coord. Chem. Rev.* **2019,** *385*, 174-190. (b) Du, M.; Li, C.-P.; Liu, C.-S.; Fan, S.-M., Design and Construction of Coordination Polymers with Mixed-Ligand Synthetic Strategy. *Coord. Chem. Rev.* **2013,** *257*, 1282–1305.
6. (a) Luo, T.-Y.; Liu, C.; Gan, X. Y.; Muldoon, P. F.; Diemler, N. A.; Millstone, J. E.; Rosi, N. L., Multivariate Stratified Metal–Organic Frameworks: Diversification Using Domain Building Blocks. *J. Am. Chem. Soc.* **2019,** *141*, 2161–2168. (b) Zhang, X.; Frey, B. L.; Chen, Y.-S.; Zhang, J., Topology-Guided Stepwise Insertion of Three Secondary Linkers in Zirconium Metal–Organic

Frameworks. *J. Am. Chem. Soc.* **2018,** *140*, 7710-7715. (c) Pang, J.; Yuan, S.; Qin, J.; Wu, M.; Lollar, C. T.; Li, J.; Huang, N.; Li, B.; Zhang, P.; Zhou, H.-C., Enhancing Pore-Environment Complexity Using a Trapezoidal Linker: Toward Stepwise Assembly of Multivariate Quinary Metal−Organic Frameworks. *J. Am. Chem. Soc.* **2018,** *140*, 12328-12332. (d) Feng, L.; Yuan, S.; Zhang, L.-L.; Tan, K.; Li, J.-L.; Kirchon, A.; Liu, L.-M.; Zhang, P.; Han, Y.; Chabal, Y. J.; Zhou, H.-C., Creating Hierarchical Pores by Controlled Linker Thermolysis in Multivariate Metal−Organic Frameworks. *J. Am. Chem. Soc.* **2018,** *140*, 2363-2372. (e) Feng, L.; Yuan, S.; Li, J.-L.; Wang, K.-Y.; Day, G. S.; Zhang, P.; Wang, Y.; Zhou, H.-C., Uncovering Two Principles of Multivariate Hierarchical Metal−Organic Framework Synthesis via Retrosynthetic Design. *ACS Cent. Sci.* **2018,** *4*, 1719-1726. (f) Sun, Y.; Sun, L.; Feng, D.; Zhou, H.-C., An In Situ One-Pot Synthetic Approach towards Multivariate Zirconium MOFs. *Angew. Chem. Int. Ed.* **2016,** *55*, 6471-6475. (g) Yuan, S.; Lu, W.; Chen, Y.-P.; Zhang, Q.; Liu, T.-F.; Feng, D.; Wang, X.; Qin, J.; Zhou, H.-C., Sequential Linker Installation: Precise Placement of Functional Groups in Multivariate Metal−Organic Frameworks. *J. Am. Chem. Soc.* **2015,** *137*, 3177-3180. (h) Burrows, A. D., Mixed-Component Metal–Organic Frameworks (MC-MOFs): Enhancing Functionality through Solid Solution Formation and Surface Modifications. *CrystEngComm* **2011,** *13*, 3623-3642.

7. (a) Kong, X.; Deng, H.; Yan, F.; Kim, J.; Swisher, J. A.; Smit, B.; Yaghi, O. M.; Reimer, J. A., Mapping of Functional Groups in Metal-Organic Frameworks. *Science* **2013,** *341*, 882-885. (b) Deng, H.; Doonan, C. J.; Furukawa, H.; Ferreira, R. B.; Towne, J.; Knobler, C. B.; Wang, B.; Yaghi, O. M., Multiple Functional Groups of Varying Ratios in Metal-Organic Frameworks. *Science* **2010,** *327*, 846-850.

8. (a) Gu, C.; Liu, J.; Hu, J.; Wang, W., Metal−Organic Frameworks Grafted by Univariate and Multivariate Heterocycles for Enhancing CO_2 Capture: a Molecular Simulation Study. *Ind. Eng. Chem. Res.* **2019**. (b) Li, S.; Chung, Y. G.; Simon, C. M.; Snurr, R. Q., High-Throughput Computational Screening of Multivariate Metal−Organic Frameworks (MTV-MOFs) for CO_2 Capture. *J. Phys. Chem. Lett.* **2017,** *8*, 6135-6141. (c) Drummond, M. L.; Cundari, T. R.; Wilson, A.

K., Cooperative Carbon Capture Capabilities in Multivariate MOFs Decorated with Amino Acid Side Chains: A Computational Study. *J. Phys. Chem. C* **2013,** *117*, 14717-14722. (d) Han, S. S.; Kim, D.; Jung, D. H.; Cho, S.; Choi, S.-H.; Jung, Y., Accurate *Ab Initio*-Based Force Field for Predictive CO_2 Uptake Simulations in MOFs and ZIFs: Development and Applications for MTV-MOFs. *J. Phys. Chem. C* **2012,** *116*, 20254-20261.

9. (a) Zhang, J.-P.; Zhang, Y.-B.; Lin, J.-B.; Chen, X.-M., Metal Azolate Frameworks: From Crystal Engineering to Functional Materials. *Chem. Rev.* **2012,** *112*, 1001−1033. (b) Pettinari, C.; Tăbăcaru, A.; Galli, S., Coordination Polymers and Metal–Organic Frameworks Based on Poly(Pyrazole)-Containing Ligands. *Coord. Chem. Rev.* **2016,** *307*, 1-31.
10. (a) Colombo, V.; Montoro, C.; Maspero, A.; Palmisano, G.; Masciocchi, N.; Galli, S.; Barea, E.; Navarro, J. A. R., Tuning the Adsorption Properties of Isoreticular Pyrazolate-Based Metal–Organic Frameworks through Ligand Modification. *J Am. Chem. Soc.* **2012,** *134*, 12830-12843. (b) Colombo, V.; Galli, S.; Choi, H. J.; Han, G. D.; Maspero, A.; Palmisano, G.; Masciocchi, N.; Long, J. R., High Thermal and Chemical Stability in Pyrazolate-Bridged Metal–Organic Frameworks with Exposed Metal Sites. *Chem. Sci.* **2011,** *2*, 1311-1319. (c) Tăbăcaru, A.; Pettinari, C.; Masciocchi, N.; Galli, S.; Marchetti, F.; Angjellari, M., Pro-porous Coordination Polymers of the 1,4-Bis((3,5-dimethyl-1H-pyrazol-4-yl)-methyl)benzene Ligand with Late Transition Metals. *Inorg. Chem.* **2011,** *50*, 11506-11513. (d) Masciocchi, N.; Galli, S.; Colombo, V.; Maspero, A.; Palmisano, G.; Seyyedi, B.; Lamberti, C.; Bordiga, S., Cubic Octanuclear Ni(II) Clusters in Highly Porous Polypyrazolyl-Based Materials. *J. Am. Chem. Soc.* **2010,** *132*, 7902–7904. (e) Galli, S.; Masciocchi, N.; Colombo, V.; Maspero, A.; Palmisano, G.; López-Garzón, F. J.; Domingo-García, M.; Fernández-Morales, I.; Barea, E.; Navarro, J. A. R., Adsorption of Harmful Organic Vapors by Flexible Hydrophobic Bis-pyrazolate Based MOFs. *Chem. Mater.* **2010,** *22*, 1664−1672.
11. (a) Herm, Z. R.; Wiers, B. M.; Mason, J. A.; van Baten, J. M.; Hudson, M. R.; Zajdel, P.; Brown, C. M.; Masciocchi, N.; Krishna, R.; Long, J. R., Separation of Hexane Isomers in a Metal-Organic Framework with Triangular Channels. *Science* **2013,** *340*, 960-964. (b) Salles, F.; Maurin, G.; Serre,

C.; Llewellyn, P. L.; Knofel, C.; Choi, H. J.; Filinchuk, Y.; Oliviero, L.; Vimont, A.; Long, J. R.; Férey, G., Multistep N_2 Breathing in the Metal−Organic Framework Co(1,4-benzenedipyrazolate). *J. Am. Chem. Soc.* **2010,** *132*, 13782–13788. (c) Zhang, J. P.; Kitagawa, S., Supramolecular Isomerism, Framework Flexibility, Unsaturated Metal Center, and Porous Property of Ag(I)/Cu(I) 3,3‘,5,5‘-Tetrametyl-4,4‘-Bipyrazolate. *J. Am. Chem. Soc.* **2008,** *130*, 907–917. (d) Park, K. S.; Ni, Z.; Côté, A. P.; Choi, J. Y.; Huang, R.; Uribe-Romo, F. J.; Chae, H. K.; O'Keeffe, M.; Yaghi, O. M., Exceptional Chemical and Thermal Stability of Zeolitic Imidazolate Frameworks. *Proc. Nat. Acad. Sci.* **2006,** *103*, 10186-10191.

12. Mosca, N.; Vismara, R.; Fernandes, J. A.; Tuci, G.; Di Nicola, C.; Domasevitch, K. V.; Giacobbe, C.; Giambastiani, G.; Pettinari, C.; Aragones-Anglada, M.; Moghadam, P. Z.; Fairen-Jimenez, D.; Rossin, A.; Galli, S., Nitro-Functionalized Bis(Pyrazolate) Metal-Organic Frameworks as Carbon Dioxide Capture Materials under Ambient Conditions. *Chem.-Eur. J.* **2018,** *24*, 13170-13180.
13. Vismara, R.; Tuci, G.; Mosca, N.; Domasevitch, K. V.; Di Nicola, C.; Pettinari, C.; Giambastiani, G.; Galli, S.; Rossin, A., Amino-Decorated Bis(Pyrazolate) Metal-Organic Frameworks for Carbon Dioxide Capture and Green Conversion into Cyclic Carbonates. *Inorg. Chem. Front.* **2019,** *6*, 533-545.
14. Pettinari, C.; Tăbăcaru, A.; Boldog, I.; Domasevitch, K. V.; Galli, S.; Masciocchi, N., Novel Coordination Frameworks Incorporating the 4,4′-Bipyrazolyl Ditopic Ligand. *Inorg. Chem.* **2012,** *51*, 5235–5245.
15. Boldog, I.; Chernega, A. N.; Sieler, J.; Domasevitch, K. V., 4,4′-Bipyrazolyl: New Bitopic Connector for Construction of Coordination Networks. *Inorg. Chim. Acta* **2002,** *338*, 69-77.
16. Coelho, A. A., Indexing of Powder Diffraction Patterns by Iterative Use of Singular Value Decomposition. *J . Appl. Crystallogr.* **2003,** *36*, 86-95.
17. TOPAS-Academic 6, Bruker, by Coelho Software, Brisbane, Australia **2016**.
18. Bond distances and angles for the rigid body describing the ligand: C-C and C-N of the pyrazole ring 1.36 Å; exocyclic C-C 1.40 Å; C-H of the pyrazole ring 0.95 Å; C-N_{NO2} 1.40 Å ; N-O 1.23 Å ;

pyrazole ring internal and external bond angles 108° and 126°, respectively; angles at the nitrogen atom of the nitro group 120°. Bond distances and angles for the rigid body describing the solvent: C-N, 1.45 Å; C-H, 0.95 Å; C-O, 1.25 Å; angles at the nitrogen and amidic carbon atoms, 120°; angles at the carbon atoms of the methyl groups, 109.5°.

19. Cheary, R. W.; Coelho, A. A., A Fundamental Parameters Approach to X-Ray Line-Profile Fitting. *J. Appl. Cryst.* **1992,** *25*, 109-121.
20. Stephens, P. W., Phenomenological Model of Anisotropic Peak Broadening in Powder Diffraction. *J . Appl. Crystallogr.* **1999,** *32*, 281-289.
21. Rouquerol, J.; Llewellyn, P.; Rouquerol, F., In *Studies in Surface Science and Catalysis*, Llewellyn, P. L.; Rodriquez-Reinoso, F.; Rouquerol, J.; Seaton, N., Eds. Elsevier Amsterdam, 2007; Vol. 160, p 49.
22. Saeidi, N.; Parvin, M., Accuracy of Dubinin-Astakhov and Dubinin-Radushkevich Adsorption Isotherm Models in Evaluating Micropore Volume of Bentonite. *Periodica Polytech., Chem. Eng.* **2016,** *60*, 123-129.
23. (a) Zhu, X.; Tian, C.; Veith, G. M.; Abney, C. W.; Dehaudt, J.; Dai, S., *In Situ* Doping Strategy for the Preparation of Conjugated Triazine Frameworks Displaying Efficient CO_2 Capture Performance. *J. Am. Chem. Soc.* **2016,** *138*, 11497–11500. (b) Zhu, X.; Mahurin, S. M.; An, S.-H.; Do-Thanh, C.-L.; Tian, C.; Li, Y.; Gill, L. W.; Hagaman, E. W.; Bian, Z.; Zhou, J.-H.; Hu, J.; Liu, H.; Dai, S., Efficient CO_2 Capture by a Task-Specific Porous Organic Polymer Bifunctionalized with Carbazole and Triazine Groups. *Chem. Commun.* **2014,** *50*, 7933-7936.
24. Schell, J.; Casas, N.; Pini, R.; Mazzotti, M., Pure and Binary Adsorption of CO_2, H_2, and N_2 on Activated Carbon. *Adsorption* **2012,** *18*, 49-65.
25. Nakamoto, K., *Infrared and Raman Spectra of Inorganic and Coordination Compounds*. 6th ed.; Wiley Press: NJ: 2009.
26. Zerbi, G.; Alberti, C., Infared Spectra of Pyrazoles- I - Pyrazoles Mono-Alkyl Substituted. *Spectrochim. Acta* **1962,** *18*, 407-423.

27. Tanabe, K. K.; Cohen, S. M., Postsynthetic Modification of Metal–Organic Frameworks - a Progress Report. *Chem. Soc. Rev.* **2011,** *40*, 498-519.

28. Bella, M.; Milata, V.; López, C.; Claramunt, R. M.; Alkorta, I.; Elguero, J., Theoretical and Experimental NMR Study of a Series of Five Nitrobenzene-1,2-Diamines. *Spectrosc. Lett.* **2013,** *46*, 91-99.

29. (a) Rossi, F.; Vioglio, P.; Chierotti, M. R.; Gobetto, R., Solid-state NMR in the Study of Intermolecular Interactions. In *Understanding Intermolecular Interactions in the Solid State: Approaches and Techniques*, Chopra, D., Ed. The Royal Society of Chemistry: 2019; pp 243-284(b) Cerreia Vioglio, P.; Chierotti, M. R.; Gobetto, R., Pharmaceutical Aspects of Salt and Cocrystal Forms of APIs and Characterization Challenges. *Adv. Drug Deliv. Rev.* **2017,** *117*, 86-110. (c) Chierotti, M. R.; Gobetto, R., Solid-state NMR Studies of Weak Interactions in Supramolecular Systems. *Chem. Commun.* **2008,** *0*, 1621-1634.

30. Blatov, V. A.; Shevchenko, A. P.; Proserpio, D. M., Applied Topological Analysis of Crystal Structures with the Program Package ToposPro. *Cryst. Growth Des.* **2014,** *14*, 3576-3586.

31. The empty volume was estimated with the software PLATON (Spek, A. L. *Acta Crystallogr. Sect. D* **2009**, *65*, 148–155) on an ordered model in *P1* for **Zn-H/NO$_2$**, **Zn-H/NH$_2$** and **Zn-NO$_2$/NH$_2$** after removal of the clathrated solvent, supposing that the nitro group protrudes into the channels. For **Zn-H/NO$_2$/NH$_2$** it was not possible to build an ordered model in *P1* symmetry, because of the discrepancy between the number of indipendent ligands of the asymmetric unit (four) and the number of different ligands of the formula unit (three). That is the reason why, for the latter, a range of porosity was estimated assigning as *minimum* the value obtained from a *P1* unit cell with one BPZ^{2-}, two $BPZNO_2^{2-}$ and one $BPZNH_2^{2-}$ as ligands in the asymmetric unit, and as *maximum* the value obtained from a *P1* unit cell with two BPZ^{2-}, one $BPZNO_2^{2-}$ and one $BPZNH_2^{2-}$ as ligands in the asymmetric unit. For all the compounds, in parenthesis, the empty volume calculated assuming that the nitro groups are coplanar to the 4,4'-bipyrazole skeleton.

32. The pore volume was calculated from the ambient conditions empty volume, supposing that the nitro group is coplanar to the 4,4'-bipyrazole skeleton.

33. Taddei, M.; Tiana, D.; Casati, N.; van Bokhoven, J. A.; Smit, B.; Ranocchiari, M., Mixed-linker UiO-66: Structure–Property Relationships Revealed by a Combination of High-Resolution Powder X-Ray Diffraction and Density Functional Theory Calculations. *Phys. Chem. Chem. Phys.* **2017,** *19*, 1551-1559.

34. Vegard, L., Die Konstitution der Mischkristalle und die Raumfüllung der Atome. *Z. Phys.* **1921,** *5*, 17-26.

35. Kleist, W.; Maciejewski, M.; Baiker, A., MOF-5 Based Mixed-Linker Metal–Organic Frameworks: Synthesis, Thermal Stability and Catalytic Application. *Thermochim. Acta* **2010,** *499*, 71-78.

36. Chavan, S. M.; Shearer, G. C.; Svelle, S.; Olsbye, U.; Bonino, F.; Ethiraj, J.; Lillerud, K. P.; Bordiga, S., Synthesis and Characterization of Amine-Functionalized Mixed-Ligand Metal–Organic Frameworks of UiO-66 Topology. *Inorg. Chem.* **2014,** *53*, 9509–9515.

37. Kandiah, M.; Nilsen, M. H.; Usseglio, S.; Jakobsen, S.; Olsbye, U.; Tilset, M.; Larabi, C.; Quadrelli, E. A.; Bonino, F.; Lillerud, K. P., Synthesis and Stability of Tagged UiO-66 Zr-MOFs. *Chem. Mater.* **2010,** *22*, 6632–6640.

38. The unusually high BET area of 916 m^2/g found for Zn($BPZNO_2$) (that does not follow the expected trend) is ascribed to the presence of defects (missing linkers?) in the MOF crystal structure. In fact, the theoretical upper limit of the BET area calculated for Zn($BPZNO_2$) through Grand Canonical Monte-Carlo simulations of the N_2 adsorption isotherm on the "defect-free" crystal structure is *much lower* than the experimental value found. For further details, please see: *Chem.-Eur. J.* **2018**, *24*, 13170 – 13180.

39. (a) Mosca, N.; Vismara, R.; Fernandes, J. A.; Casassa, S.; Domasevitch, K. V.; Bailón-García, E.; Maldonado-Hódar, F. J.; Pettinari, C.; Galli, S., CH_3-Tagged Bis(pyrazolato)-Based Coordination Polymers and Metal–Organic Frameworks: an Experimental and Theoretical Insight. *Cryst. Growth Des.* **2017,** *17*, 3854–3867. (b) Nugent, P.; Belmabkhout, Y.; Burd, S. D.; Cairns, A. J.; Luebke, R.;

Forrest, K.; Pham, T.; Ma, S.; Space, B.; Wojtas, L.; Eddaoudi, M.; Zaworotko, M. J., Porous Materials with Optimal Adsorption Thermodynamics and Kinetics for CO_2 Separation. *Nature* **2013,** *495*, 80-84.

40. (a) Liu, B.; Zhou, H.-F.; Hou, L.; Wang, Y.-Y., Functionalization of MOFs via a Mixed-Ligand Strategy: Enhanced CO_2 Uptake by Pore Surface Modification. *Dalton Trans.* **2018,** *47*, 5298–5303. (b) McDonald, T. M.; D'Alessandro, D. M.; Krishna, R.; Long, J. R., Enhanced Carbon Dioxide Capture upon Incorporation of N,N′-Dimethylethylenediamine in the Metal–Organic Framework CuBTTri. *Chem. Sci.* **2011,** *2*, 2022-2028.
41. Even though counterintuitive, the quantity of CO_2 adsorbed by **Zn-H/NO₂** at 298 K is *higher* than that at 273 K. The behaviour is reproducible, and it has been checked on a number of different samples. The reason may be ascribed to a different orientation of the nitro groups in the channels that reduces the empty volume at 273 K.

TOC Graphic